

Article

Thermal Properties and Behaviour of Am-Bearing Fuel in European Space Radioisotope Power Systems

Emily Jane Watkinson ^{1,2,*}, Ramy Mesalam ², Jean-François Vigier ¹, Ondřej Beneš ¹, Jean-Christophe Griveau ¹, Eric Colineau ¹, Mark Sierig ¹, Daniel Freis ¹, Richard M. Ambrosi ², Dragos Staicu ¹ and Rudy J. M. Konings ¹

¹ Joint Research Centre (JRC), European Commission, P.O. Box 2340, 76125 Karlsruhe, Germany; Jean-Francois.VIGIER@ec.europa.eu (J.-F.V.); Ondrej.BENES@ec.europa.eu (O.B.); Jean-Christophe.GRIVEAU@ec.europa.eu (J.-C.G.); Eric.COLINEAU@ec.europa.eu (E.C.); Mark.SIERIG@ec.europa.eu (M.S.); Daniel.FREIS@ec.europa.eu (D.F.); Dragos.STAICU@ec.europa.eu (D.S.); Rudy.KONINGS@ec.europa.eu (R.J.M.K.)

² School of Physics and Astronomy, University of Leicester, University Road, Leicester LE1 7RH, UK; rm558@leicester.ac.uk (R.M.); rma8@leicester.ac.uk (R.M.A.)

* Correspondence: ejw38@leicester.ac.uk

† Visiting Scientist.

Abstract: The European Space Agency is funding the research and development of ²⁴¹Am-bearing oxide-fuelled radioisotope power systems (RPSs) including radioisotope thermoelectric generators (RTGs) and European Large Heat Sources (ELHSs). The RPSs' requirements include that the fuel's maximum temperature, T_{max} , must remain below its melting temperature. The current prospected fuel is (Am_{0.80}U_{0.12}Np_{0.06}Pu_{0.02})O_{1.8}. The fuel's experimental heat capacity, C_p , is determined between 20 K and 1786 K based on direct low temperature heat capacity measurements and high temperature drop calorimetry measurements. The recommended high temperature equation is $C_p(T/K) = 55.1189 + 3.46216 \times 10^2 T - 4.58312 \times 10^5 T^{-2}$ (valid up to 1786 K). The RTG/ELHS T_{max} is estimated as a function of the fuel thermal conductivity, k , and the clad's inner surface temperature, $T_{i,cl}$, using a new analytical thermal model. Estimated bounds, based on conduction-only and radiation-only conditions between the fuel and clad, are established. Estimates for k (80–100% T.D.) are made using C_p , and estimates of thermal diffusivity and thermal expansion estimates of americium/uranium oxides. The lowest melting temperature of americium/uranium oxides is assumed. The lowest k estimates are assumed (80% T.D.). The highest estimated T_{max} for a 'standard operating' RTG is 1120 K. A hypothetical scenario is investigated: an ELHS $T_{i,cl} = 1973$ K—the RPSs' requirements' maximum permitted temperature. Fuel melting will not occur.

Keywords: americium; heat capacity; radioisotope power systems



Citation: Watkinson, E.J.; Mesalam, R.; Vigier, J.-F.; Beneš, O.; Griveau, J.-C.; Colineau, E.; Sierig, M.; Freis, D.; Ambrosi, R.M.; Staicu, D.; et al.

Thermal Properties and Behaviour of Am-Bearing Fuel in European Space Radioisotope Power Systems. *Thermo* **2021**, *1*, 297–331. <https://doi.org/10.3390/thermo1030020>

Academic Editor: Johan Jacquemin

Received: 30 June 2021

Accepted: 8 October 2021

Published: 15 October 2021

Publisher's Note: MDPI stays neutral with regard to jurisdictional claims in published maps and institutional affiliations.



Copyright: © 2021 by the authors. Licensee MDPI, Basel, Switzerland. This article is an open access article distributed under the terms and conditions of the Creative Commons Attribution (CC BY) license (<https://creativecommons.org/licenses/by/4.0/>).

1. Introduction

Since 2008, the European Space Agency (ESA) has funded a research and development (R&D) programme to develop European radioisotope power systems (RPSs), specifically radioisotope thermoelectric generators (RTGs), Stirling generators and radioisotope heater units (RHUs). These systems will enable the exploration of some of the most challenging environments in our solar system, i.e. those that are inaccessible or highly restricted by using solar array electrical power systems [1–4]. The RTG contains an internal modular 'heat source' known as the European Large Heat Source (ELHS). This is effectively a large RHU that can be used as a standalone RPS. A detailed ESA study identified and concluded that ²⁴¹Am is the most economically viable option for Europe to use for European RPSs [1]; the United Kingdom has heritage in reprocessing civil nuclear fuel, which has resulted in civil plutonium stockpiles that now contain a significant mass of ingrown ²⁴¹Am [5].

The ESA has also been funding fundamental fuel form development research since the onset of the programme. Sarsfield et al. developed a novel process to chemically extract

^{241}Am from the Pu and transform the Am into a very high purity oxide, namely AmO_2 . This is known as the Americium and Plutonium Purification by Extraction (AMPPEX) process and it can be adapted to produce Am_2O_3 [5]. Prior to this, several investigations were conducted to understand (1) how to synthesise surrogates for different americium oxides (using oxalate precipitation and calcination routes) and (2) how to adjust their particle characteristics [6,7]. Several sintering investigations with surrogates for americium fuel (CeO_2 , Nd_2O_3) were also pursued in 2015 to 2016 [6,8]. Targeted sintered properties included handling strength, and a relative theoretical density of 85–90% to allow sufficient porosity for helium outgassing [8]. That study highlighted the need to make pellets that remain integral [8].

In 2016, high purity AmO_2 material made by the AMPPEX process was used for the first ^{241}Am sintering trial of the ESA programme [9]. This was a joint study between the National Nuclear Laboratory (UK) and the European Commission Joint Research Centre (JRC) in Karlsruhe [9]. In general, the AmO_2 material was pressed, and reduced to Am_2O_3 during the sintering process [9]. Small sintered americium oxide discs (~4.25 to 4.50 mm ϕ) with relative densities within or close to the target range were made [9]. However, many discs experienced cracking [9]. One possible cause for the cracking was the change in crystal structure from cubic to hexagonal form as the AmO_2 was reduced to Am_2O_3 [9]; AmO_2 has a tendency to reduce above 1100 K even in air [10]. Consequently, Vigier et al. (JRC Karlsruhe) [11] embarked on a study to produce an americium based oxide with a cubic crystal structure that remained cubic during sintering. They created an americium oxide stabilised with a small fraction of uranium (12%) [11]. They were able to sinter intact discs/pellets, i.e. without cracks [11]. The material was synthesised via the JRC gel supported co-precipitation route and they successfully pressed and sintered multiple small discs and a larger pellet [11]. Each was close to the target density, integral, and maintained structural stability over time [11]. Relative densities of up to 93% T.D. were achieved [11].

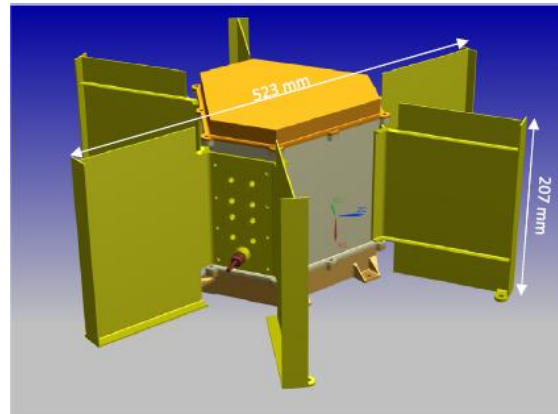
The University of Leicester is designing and manufacturing the European RHU, the RTG and the ELHS. Its RTG R&D dates back to 2010. These systems have undergone several design iterations with safety at their forefront whilst enabling their specific thermal and specific electrical power performances and manufacturability to be improved. A more recent design of the European RTG is illustrated in Figure 1, with the external view shown in Figure 1a. It comprises multiple safety subsystems including the Pt-20%Rh clads that are shown in Figure 1b. These clads contain the sintered americium uranium oxide fuel. For each of the RPSs, the Pt-20%Rh clad is the inner most containment layer. The fuel will be a cylindrical stack of discs or a single cylindrical pellet of equivalent volume. The article by Ambrosi et al. describes in detail the design evolutions (up to 2019) of the RHU, ELHS and RTG systems with explanations of the safety-led design features [4]. The University of Leicester's most recent RHU, ELHS and RTG designs assume the fuel to be $(\text{Am}_{0.80}\text{U}_{0.12}\text{Np}_{0.06}\text{Pu}_{0.02})\text{O}_{1.8}$ [4] developed by Vigier et al. [11].

Understanding the temperature distribution across each type of RPS under different conditions is essential for assessing and evolving their designs. Thermal models of the systems are, therefore, important. Under the European RPS R&D programme, finite element (FE) thermal models have been and will be developed.

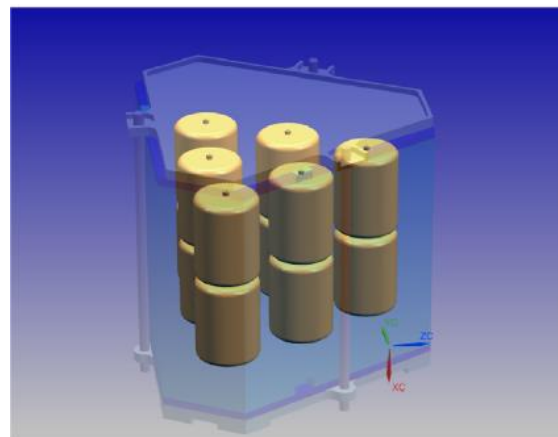
The University of Leicester is developing the requirements for each of the RPSs (RHU, ELHS and RTG) for the ESA programme [12]. These are regularly reviewed as the systems' designs evolve. For all RPSs, the fuel is required to not reach its melting point. Provided that the thermal conductivity of the fuel is known, thermal models can be used to determine the maximum temperature of the fuel in an RPS (under a given condition). It can then be assessed if the maximum temperature of the fuel is less than its melting temperature. Therefore, the thermal conductivity of the new prospect RPS fuel, $(\text{Am}_{0.80}\text{U}_{0.12}\text{Np}_{0.06}\text{Pu}_{0.02})\text{O}_{1.8}$, is an essential property that needs to be determined.

As the RTG contains an ELHS (the latter contains the fuel), the two systems can often be considered together. The different designs of the RTG/ELHS and RHU systems result in an inherently hotter fuel in the RTG/ELHS than in the RHU. Therefore, it is most key to

assess the maximum fuel temperature in RTG/ELHS rather than in an RHU for a given environment. Each of the RPSs has a requirement that imposes a temperature limit on the clad(s) [12]. Specifically, the temperature of a clad (for any RPS) must not be greater than 200 K below its melting temperature [12], i.e. the clad's temperature must not exceed 1973 K. This is based on a Pt-20%Rh clad, which is assumed to have a 2173 K melting temperature [13].



(a)



(b)

Figure 1. (a) The RTG casing and radiator fins and (b) an illustration of the Pt-20%Rh inside the RTG that encapsulates the Am-U oxide fuel. This image is reprinted from [4] (see reference for the required creative commons license link).

Other temperature limits related to the fuel/clad include a potential minimum temperature at which the fuel and clad could chemically interact. The literature suggests that Pt and Rh can each react with americium oxides under certain conditions [14,15]. In 2019, Ambrosi et al. reported initial indications of temperatures that should not be exceeded for the RPSs [4]. The temperatures that referred to the fuel, e.g. fuel melting temperature, were based on data for AmO₂ or Am₂O₃ (previous RPS fuel candidates) and new data for the Am-U oxide will be required to revise these [4]. As an example, an ongoing investigation is being pursued by Watkinson et al. to determine if there is a chemical interaction between (Am_{0.80}U_{0.12}Np_{0.06}Pu_{0.02})O_{1.8} and Pt-20%Rh and other Pt-Rh alloys at different temperatures including elevated temperatures [16]. Although compatibility tests at only 200 °C have been reported so far [16], the study aims to investigate the materials' interaction up to 1650 °C. Temperature limits of the RPSs associated with fuel-clad chemical interactions will not be discussed further in this study.

It is also important to determine the heat capacity of (Am_{0.80}U_{0.12}Np_{0.06}Pu_{0.02})O_{1.8} as a function of temperature. Based on the very few experimental facilities available

worldwide to analyse americium-based materials, the key route for determining their thermal conductivities as functions of temperature is by using heat capacity measurements (transformed to specific heat capacity data) and thermal diffusivity measurements. Heat capacity data may also be useful for the future determination (or improvement) of the Am-U-oxide phase diagram. Specific heat capacity data will be needed for transient thermal modelling of the RPS systems under different conditions in the future.

Epifano et al. [17] reported experimental heat capacity data for $(U, Am)O_{2\pm x}$ with $Am/[Am+U]$ ratios from 0.32 to 0.68 and Vălu et al. reported data for $(U_{1-y}, Am_y)O_{2-x}$ with y values of 0.0877 and 0.1895 and x values of 0.01 to 0.03 [18]. Both sets of materials were investigated in the context of transmutation target fuels for next generation reactors [17,18]. Nishi et al. [19] reported data for Am_2O_3 and AmO_2 up to ~ 1080 K. There are, therefore, only a handful of papers describing the heat capacities of materials similar to the new fuel for the European radioisotope power systems. However, there are no experimental data in the literature for a mixed uranium americium oxide that comprises as high an $Am/(Am+U)$ ratio as this prospected ESA fuel, i.e. 0.80. Recently, Jossu et al. [20] published a theoretical investigation into the variation of the heat capacity of $(U, Am)O_2$ with different Am contents, including concentrations that came close to $(Am_{0.80}U_{0.12}Np_{0.06}Pu_{0.02})O_{1.8}$. Experimental data for high Am contents would help to validate this data for this region. An experimental investigation is key to characterising this novel material for this space application. The results of this study may also be of interest to the wider nuclear fuels community regarding thermal properties of Am containing transmutation targets with high Am contents. They may also be of interest as an alternative system to other mixed oxides transmutation targets. For example, Bromley and Colton [21] investigated the use of Am-Th oxides as transmutation targets in blanket fuels as an alternative to AmO_2 . They noted that Am-Th oxides are preferable to AmO_2 because the latter reduces at higher temperatures (to O/Am ratios less than 2), causing an unwanted reduction in thermal conductivity.

The first objective of this paper is to experimentally characterise the heat capacity of $(Am_{0.80}U_{0.12}Np_{0.06}Pu_{0.02})O_{1.8}$ as a function of temperature as a step towards characterising the thermal conductivity of the fuel. Drop calorimetry will be used to determine its enthalpy increment variation with temperature. The high temperature heat capacity of this fuel as a function of temperature will be determined using this enthalpy data and low temperature heat capacity data (the details of this process will be explained in Section 2.1).

The second objective of this study considers the fuel in context of the RPSs. The objective is to investigate if a $(Am_{0.80}U_{0.12}Np_{0.06}Pu_{0.02})O_{1.8}$ fuel with different relative densities (80–100%) could reach a melting temperature when in its clad is at 1973 K—the maximum permitted temperature imposed by the current RPSs' requirements [12]. This is a hypothetical scenario where the fuelled clad (in a steady-state scenario) would be exposed to an external heat source that causes the clad to be at 1973 K. An 80% T.D. to 100% T.D. fuel is the likely maximum range of relative densities that could be considered in the RPS programme when considering all aspects of the fuel's design, e.g. thermal power density, and He outgassing considerations. Therefore, with respect to He outgassing, an even lower relative density of 80% T.D. is considered here than the 85% T.D. that was the lowest option considered previously.

It is noted that as the RTG/ELHS fuel is always hotter than the RHU fuel, the geometry and properties of the ELHS/RTG will be considered. In fact, in such a scenario, the outer parts of the RTG would unlikely be present and, therefore, the ELHS can be referred to. To enable this objective to be investigated, the experimental heat capacity data for $(Am_{0.80}U_{0.12}Np_{0.06}Pu_{0.02})O_{1.8}$ and assumptions for thermal diffusivity and thermal expansion data of similar oxides will be used to estimate a range of possible thermal conductivities of the fuel. This study will specifically focus on the lowest estimate for the thermal conductivity of this fuel and the lowest melting temperature of similar fuels in the literature. This method of analysis is, therefore, more conservative in assessing the possibility of fuel melting. Melting temperature data for $(Am_{0.80}U_{0.12}Np_{0.06}Pu_{0.02})O_{1.8}$ is yet to be

determined. Therefore, the melting temperatures of similar oxides will be reviewed and the lowest value will be assumed for this study. A new analytical thermal model will be developed to determine the maximum temperature of the fuel as a function of fuel thermal conductivity and clad temperature. The existing long-standing finite element (FE) thermal model for the RTG developed by the University of Leicester is used to understand its temperature distribution under standard operation conditions. However, due to the long time period needed to reach a solution, this model does not allow the effect of different specific clad temperatures on the maximum fuel temperature to be investigated easily.

The ELHS and RHU clad designs provide additional volume within their clads to allow the fuel to expand with some margin. The heat transfer between the outer surface of the fuel and the inner surface of the clad will be via conduction (if the surfaces are in contact) and/or via radiation (if not). Convection is neglected. In practice, the heat transfer will be a combination of both routes. The analytical thermal model will be used to estimate an envelope of possible maximum fuel temperatures for a given clad temperature and fuel thermal conductivity. The lower estimate will correspond to conduction-only heat transfer between the fuel and the clad, and the upper estimate will correspond to radiation-only heat transfer.

The development of the RPSs is on a targeted timeline. Specifically, they are being developed for future ESA missions that will launch into space from the late 2020s onwards. Conducting the second objective's investigation now is very informative to the RPS R&D programme. Specifically, it provides the opportunity for immediate critical reflection of the current designs and requirements [12] of the RTG/ELHS, its fuel and of the RHU. It allows this to be conducted using the lowest estimates for the fuel thermal conductivity and, therefore, prior to determining its precise thermal conductivity. Precise thermal conductivity data will likely be required for more detailed finite element thermal models in the future.

In summary, this paper presents (1) an experimental study to determine the heat capacity of the $(\text{Am}_{0.80}\text{U}_{0.12}\text{Np}_{0.06}\text{Pu}_{0.02})\text{O}_{1.8}$ for the first time, and (2) a study that utilises this data to estimate the potential impact on the maximum temperature of the fuel in the (a) RTG during operation and (b) in an ELHS fuelled clad that is at 1973 K to assess if fuel melting could occur.

2. Experiment

The data will be compared to experimental data for americium oxides and americium-uranium mixed oxides. A large range of temperatures are experimentally investigated up to 1785 K. This large range will likely include the operating temperatures of RTG fuel (the value will be estimated in this study). Understanding the RHU and RTG fuels' potential performances under operational and non-operational conditions is paramount for space mission nominal performance and safety performance. Specifically, here, the enthalpy increment as a function of temperature will be measured using drop calorimetry for this Am-U oxide to then determine its heat capacity as a function of temperature. Additionally, the heat capacity of the material will be characterised at low temperatures, and the obtained values will be used to constrain the required fit for the heat capacity data to realistic limits. This provides greater confidence in the fit for heat capacity as a function of temperature for the temperatures of interest.

In summary, this part of this study presents (1) heat capacity measurements as a function of temperature between 20 K and 249 K, (2) drop calorimetry enthalpy increment measurements as a function of temperature from 430 K to 1786 K and (3) the transformation of the latter data and its fitting to develop a realistically lower temperature constrained heat capacity as a function of temperature.

2.1. Materials and Methods

The initial powder was prepared by gel-supported co-precipitation in ammonia. This method is known to provide homogeneous powders without the need of a ball milling

step [22]. The material was dried, calcined at 1073 K, pressed into discs at 400 MPa and sintered under Ar/4% H₂/2000 ppm H₂O at 1873 K. One large pellet of about 3 g and five small discs were produced during this synthesis. This material was made by Vigier et al. [11] and details about the synthesis and characterisation of this material can be found in their article, where it is referred as 'batch #5' [11]. For completeness, some details of how they characterised its composition are provided here in brief as well as details of its structure (according to Vigier et al. [11]). Vigier et al. oxidised some of the sintered sample in a thermogravimetric analysis instrument to determine its oxygen to metal ratio. They used electron probe microanalysis to determine the Am, U, Np and Pu compositions [11]. The sintered material had a composition of (Am_{0.80}U_{0.12}Np_{0.06}Pu_{0.02})O_{1.8} (The actinides correspond to ²⁴¹Am, ²³⁷Np and ²³⁹Pu, and natural uranium was used [11]). In fact, the Np and Pu are impurities in the material, as noted by Vigier et al. [11]. They arose from the americium source material used by Vigier et al. [11]. The material had a cubic crystal structure (*Ia-3* space group) with an 11.02535(5) Å lattice parameter (further structural details are found in the article by Vigier et al. [11]).

One of the five discs was broken into fragments for heat capacity measurement purposes. Two fragments of 8.86 mg and 2.26 mg were used for low temperature heat capacity measurements, and three fragments of 34 mg, 46 mg and 48 mg were used for drop calorimetry measurements.

2.1.1. Low Temperature Heat Capacity Measurements

The heat capacity of (Am_{0.80}U_{0.12}Np_{0.06}Pu_{0.02})O_{1.8} was measured using a low-temperature vacuum calorimeter based on a hybrid adiabatic relaxation method (PPMS-9T, Quantum Design Inc.) as described in a previous paper [23], with estimated uncertainties for the heat capacities as reported by Lashley et al. [24]. Samples were wrapped in Stycast 2850 FT epoxy glue for α -contamination protection reasons [25]. A small amount of thermal grease APIEZON[®] N was used to ensure good thermal contact between the wrapped sample and the sapphire platform of the measurement support (puck). For each sample, the total heat capacity contribution of the puck and grease attached to the sample was determined. The heat capacity of the sample was determined by subtracting the heat capacity contributions of the Stycast epoxy 2850 FT and of the combined puck and grease from the overall heat capacity measurement of the system. The heat capacity of the Stycast epoxy 2850 FT as a function of temperature per unit mass was well calibrated in previous studies [26]. This was conducted using Quantum Design Multiview software. Measurements were performed on two pieces of sintered (Am_{0.80}U_{0.12}Np_{0.06}Pu_{0.02})O_{1.8} material that were 2.26 mg and 8.86 mg. These were wrapped in 1.12 mg and 7.96 mg of Stycast, respectively, and measurements were taken between around 2 K to 250 K. Self-heating of ²⁴¹Am ($Q = 114 \text{ mW g}^{-1}$), which is the main heat contributor in the material, leads to a minimum temperature of 19 K on the sample, even for the lowest mass sample. A specific procedure to remove self-heating effect was applied to estimate the real temperature of the sample [26]. All measurements were performed under high vacuum ($\sim 10^{-4}$ Pa) in the sample chamber.

Further details of the encapsulation method and of the calibration method can be found in Lashley et al. [24].

2.1.2. Drop Calorimetry for Enthalpy Increment Measurements with Temperature

A Setaram Multi Detector High Temperature Calorimeter (MDHTC-96 type) functioning in 'drop mode' was used to collect the enthalpy increment measurements for the samples. As is the case with much of the apparatus at JRC-Karlsruhe, the calorimeter has been adapted to allow radioactive samples to be tested [18]. The calorimeter is housed in a glovebox whilst the majority of its electronics are external. This is essential and key to minimise end of instrument-life nuclear waste and to aid system maintenance [18,27]. Details of the configuration of the calorimeter are provided by Beneš [28]. The drop calorimeter uses a graphite furnace. This requires flowing inert gas to minimise its oxidation [28].

Helium was used in this experiment. The temperature measurement of the calorimeter was calibrated across its range using a variety of metal standards with a series of melting points [18,28]. Measurements were taken under ambient pressure conditions.

The concept and method of drop calorimetry measurements are concisely described by Beneš et al. [27] and Epifano et al. [17]. For completeness, the key points are outlined in the following paragraphs:

When a sample is dropped in a calorimeter from ambient temperature to the detector region that is at a constant higher temperature, a thermal shock is created in the region of the detector, i.e. it cools to a lower temperature. Consequently, the furnace responds by adding heat to the detector region to maintain the original temperature. Drop calorimetry is used to measure enthalpy increments at different temperatures. In the case of radioactive samples, corrections are required for self-heating contributions. A corrected enthalpy increment versus temperature curve is produced. By definition, the heat capacity, C_p , as a function of temperature, is the derivative of the enthalpy function with respect to temperature. This allows C_p to be determined.

Reference samples are non-radioactive and have well-characterised heat capacity–temperature relationships. Reference samples are dropped in the calorimeter to calibrate the heating response of the furnace (a voltage signal) with the actual enthalpy increment of the reference material. This corresponds to the heat contribution of the furnace to maintain temperature equilibrium. This is conducted for the measurement temperatures of interest. Here, four pieces of platinum (99.95% Pt, Goodfellow Cambridge Ltd., Huntingdon, UK) were used as reference materials for the three Am-U oxide samples dropped in the calorimeter (Comparative enthalpy increment measurement tests were routinely conducted between platinum and sapphire (another reference material) to check for discrepancies between the two reference materials. None were observed, which provided confidence in the use of platinum as a reference material.). A reference material was dropped before and after each sample to allow the average response of the heating system to be accounted for. Fortunately, the samples could be pre-loaded into a carousel that allowed automatic dropping of the samples approximately every 25 min after the apparatus had equilibrated to the required temperature for measurement. However, the temperature profile of the apparatus was pre-programmed and took approximately 7 h to stabilise before any dropping commenced. The masses of each sample were recorded prior to them being loaded into the carousel and were measured once again after the drops were completed to provide an initial indication of any small stoichiometry change. Here, each Am-U oxide sample was sufficiently hard to not break at the end of each drop in the calorimeter. This aided measuring the sample masses post-drop.

The physics of the above explanation can be considered mathematically [17,28]. Before the molar enthalpy increments of the sample measured at a given temperature can be determined, a sensitivity factor, S , needs to be established. It is calculated based on the drop of a reference material:

$$S = \frac{M_r}{m_r} \frac{\int_{t_1}^{t_2} \varnothing_r dt}{\int_{T_{amb}}^{T_{mes}} C_{p,r}(T) dT} \quad (1)$$

where M_r and m_r are the molar mass and mass of the reference material, respectively, T_{mes} and T_{amb} are the measurement and ambient temperatures, respectively, $\int_{t_1}^{t_2} \varnothing_r dt$, is the time integrated peak heat-flow associated with the drop of the reference sample (over the time interval $t_2 - t_1$), and the denominator is the molar enthalpy increment resulting from the drop of the reference sample from ambient temperature to the measured temperature. Finally, $C_{p,r}$ is the heat capacity of the reference material, which is well characterised for the said reference material as a function of temperature T .

The enthalpy increment (molar), ΔH_m , of the sample when it is dropped from ambient temperature to the measurement temperature is then [17]:

$$\frac{T_{mes}}{T_{amb}} \Delta H_m = \frac{M_s}{m_s} \frac{\int_{t_i}^{t_f} \varnothing_s dt}{S} + D \quad (2)$$

where M_s the molar mass of the sample, m_s is the mass of the sample and $\int_{t_i}^{t_f} \varnothing_s dt$ is the time integrated peak heat-flow for the sample (over the interval $t_f - t_i$), which corresponds to the area of peak heat-flow for a given drop. S is the sensitivity factor based on the reference material's dropped before and after the sample and is calculated using Equation (1). Finally,

$$\begin{aligned} D &= 0 && \text{for a non-radioactive sample} \\ &= Q_\alpha p m_s (t_f - t_i) && \text{for an alpha emitting sample,} \end{aligned} \quad (3)$$

where Q_α is the self-generated heat produced from the alpha decay of the material, p is the specific power of the material, which is 0.082 mW mg^{-1} for the Am-U oxide [11], m_s is the mass of the sample and the final term is the time interval for the peak heat-flow [17].

As the Am-U oxide samples were aged, it was possible that self-irradiation defects could be annealed at higher temperatures during drop calorimetry. This point was also raised by Epifano et al. [17]. They noted that latent heat could be released during annealing causing an uncertainty in enthalpy increment measurements [17]. Three steps were conducted to reduce the likelihood of this happening. Firstly, the three samples were heated using the drop calorimeter at 1573 K to anneal defects for future measurements. These data were not used. Subsequently, the samples were assumed to be defect-free. Secondly, the analysis was conducted over a short period of time (a few weeks), and, finally, the temperature was alternated between higher and lower temperatures between each set of drops to help avoid the accumulation of irradiation defects.

2.1.3. Fitting Method

The heat capacity of a material is defined as the derivative of its enthalpy function with respect to temperature. A method similar to that presented by Beneš et al. [27] for NpO_2 was used to determine the heat capacity equation. Specifically, the low temperature heat capacity measurements (presented in Section 2.2.1) and the high temperature molar enthalpy increments (Section 2.2.2) were fitted using a simultaneous least squares linear regression to the well-known Maier-Kelly formula for heat capacity variation with temperature:

$$C_p = a + bT + cT^{-2} \quad (4)$$

where a , b and c were constants to be determined by the fitting procedure. The fit was constrained by the low temperature data for heat capacity variation as function of temperature. This therefore allowed the high temperature data for heat capacity variation to be fitted without the need to assume values for the lower temperature heat capacity, e.g. based on the Neumann-Kopp additive rule and known heat capacity data for AmO_2 and UO_2 .

2.2. Results

2.2.1. Low Temperature Heat Capacity Measurements

The low temperature heat capacity was measured for two independent samples from the lowest achievable temperatures up to 250 K. The combined results of both measurements are shown in Figure 2. Due to the decay-heat generated by americium, it was not possible to reach a temperature lower than 19 K.

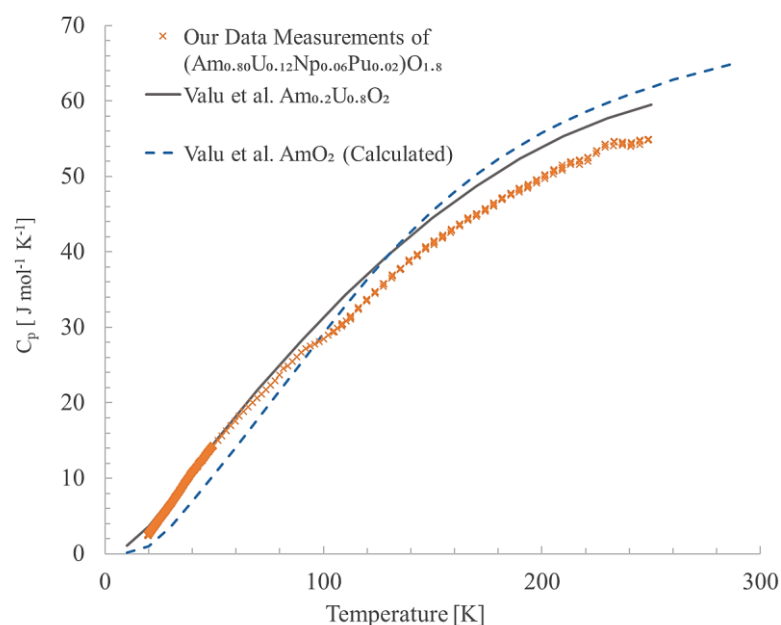


Figure 2. The low temperature heat capacity measurement recorded for two $(\text{Am}_{0.80}\text{U}_{0.12}\text{Np}_{0.06}\text{Pu}_{0.02})\text{O}_{1.8}$ samples. The data are combined. Data for $\text{Am}_{0.2}\text{U}_{0.8}\text{O}_2$ and AmO_2 from Valu et al. [23] are also plotted for comparison.

Figure 2 also illustrates the low temperature heat capacity data of $\text{Am}_{0.2}\text{U}_{0.8}\text{O}_2$ and AmO_2 from Valu et al. [23]. The figure illustrates that the $(\text{Am}_{0.80}\text{U}_{0.12}\text{Np}_{0.06}\text{Pu}_{0.02})\text{O}_{1.8}$ data are more comparable to $\text{Am}_{0.2}\text{U}_{0.8}\text{O}_2$ than to AmO_2 . This indicates that the triple doping of U, Np and Pu may have a significant influence. Unlike UO_2 [29], NpO_2 [30] and their related systems, $\text{U}_{1-x}\text{Np}_x\text{O}_2$ [29,31], the $(\text{Am}_{0.80}\text{U}_{0.12}\text{Np}_{0.06}\text{Pu}_{0.02})\text{O}_{1.8}$ data do not indicate the presence of a magnetic phase transition. UO_2 orders antiferromagnetically at $T_N = 31$ K [29] and NpO_2 exhibits multipolar ordering below $T_0 = 26$ K [30].

Figure 2 illustrates a slight anomaly at around 100 K. This corresponds to the mathematical overcorrection by the Q.D. Multiview software was used to subtract the combined platform (puck) and grease heat capacity contribution (resulting in a $\sim 2\%$ uncertainty in the heat capacity). Thermal coupling between the sample and the platform decreased to below 80% above 260 K. A vitreous–liquid phase transition is usually observed for APIEZON[®] N grease above 260 K under vacuum. It cannot be fully subtracted from the total contribution with the sample. Data at temperatures greater than 260 K were less reliable for strong self-heating samples (^{241}Am or ^{238}Pu based materials). Therefore, in conclusion, only data below 260 K are considered here, as shown in Figure 2.

The low temperature heat capacity was found to fit well with a combination of Einstein and Debye solid functions. Details of this can be found in Appendix A.

2.2.2. High Temperature Enthalpy Increment Measurements

The average of each set of three molar enthalpy measurements taken at each high temperature is shown in Table 1 together with their standard deviations for $(\text{Am}_{0.80}\text{U}_{0.12}\text{Np}_{0.06}\text{Pu}_{0.02})\text{O}_{1.8}$. These results are plotted in Figure 3 together with its fitted curve. The explanation of how this curve was determined will be explained. These results are compared to experimentally derived data (and their extrapolations) in the literature for AmO_2 (Nishi et al.), UO_2 (Fink et al. and Valu et al.) and $\text{U}_{0.3}\text{Am}_{0.7}\text{O}_{2\pm x}$ (Epifano et al.), reported in references [17–19,32], in Figure 3a–c, respectively.

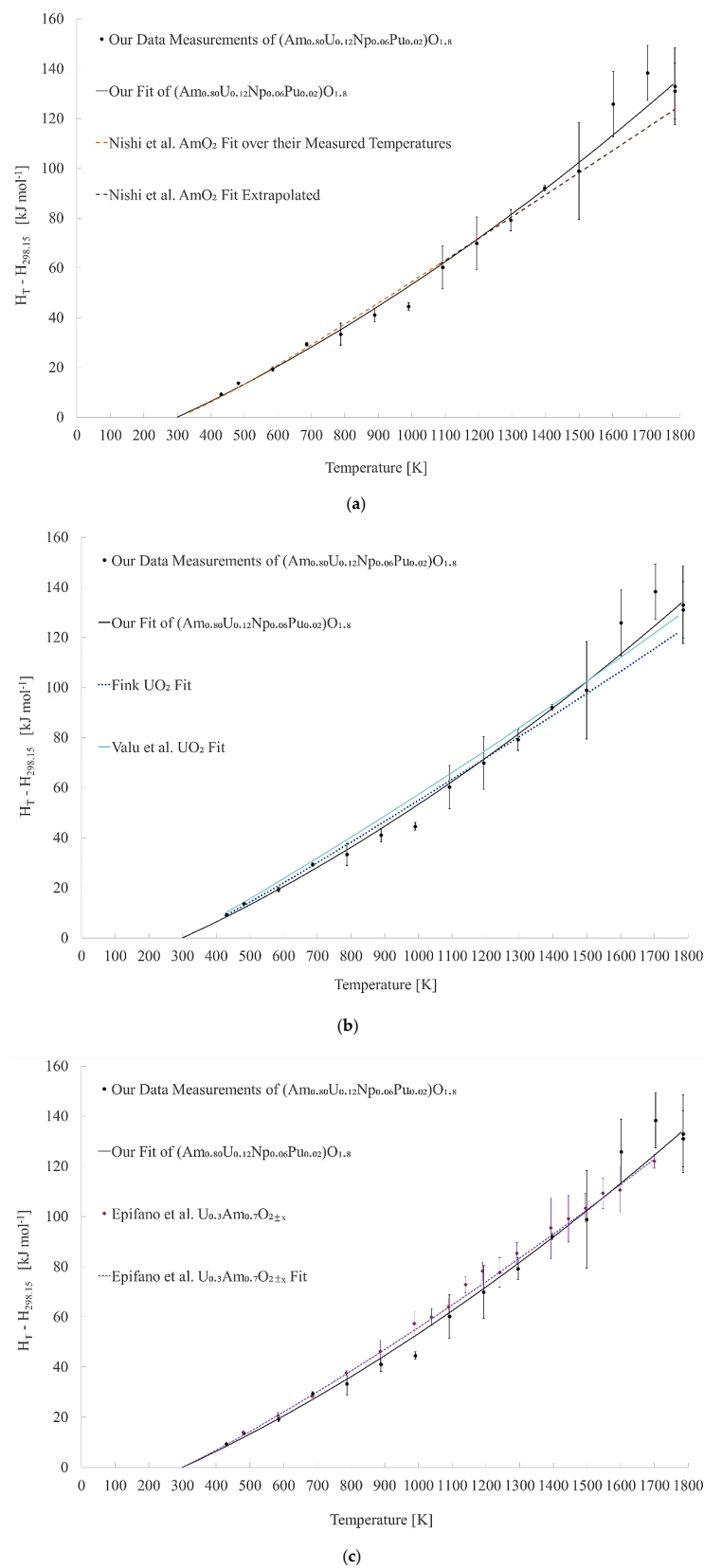


Figure 3. The high temperature molar enthalpy heat measurements determined by drop calorimetry for our Am-U oxide $(\text{Am}_{0.80}\text{U}_{0.12}\text{Np}_{0.06}\text{Pu}_{0.02})\text{O}_{1.8}$ under helium shown in black in (a–c). For comparison, (a) the AmO_2 data by Nishi [14] et al. and its extrapolation, (b) various data for UO_2 by Valu [18] and Fink [32] and (c) the $\text{U}_{0.3}\text{Am}_{0.7}\text{O}_{2\pm x}$ data recorded under air by Epifano et al. [17].

The fitted parameters of Equation 4 for $(\text{Am}_{0.80}\text{U}_{0.12}\text{Np}_{0.06}\text{Pu}_{0.02})\text{O}_{1.8}$ are outlined in Table 2. This curve is plotted together with the low temperature heat capacity data in Figure 4. It also illustrates data for UO_2 , AmO_2 and $\text{U}_{0.3}\text{Am}_{0.7}\text{O}_{2\pm x}$ for comparison. Furthermore, by definition, the integral of Equation 4 with respect to temperature is the change in enthalpy increments as a function of temperature. These data for $(\text{Am}_{0.80}\text{U}_{0.12}\text{Np}_{0.06}\text{Pu}_{0.02})\text{O}_{1.8}$ are plotted in Figure 3.

Table 1. The average high temperature enthalpy increments ΔH_m of the Am-U oxide, $(\text{Am}_{0.80}\text{U}_{0.12}\text{Np}_{0.06}\text{Pu}_{0.02})\text{O}_{1.8}$, samples at different temperatures. The uncertainty provided is the standard deviation of the measurements.

T_{mes} (K)	ΔH_m	$\frac{T_{mes}}{T_{am}}$	(J mol ⁻¹)
430	9329	±	348
482	13693	±	403
585	19353	±	1024
686	29360	±	690
788	33335	±	4388
889	41078	±	2752
990	44580	±	1463
1092	60247	±	8622
1193	69876	±	10535
1295	79186	±	4252
1397	92012	±	1183
1499	98868	±	19447
1601	125802	±	13072
1703	138306	±	11035
1785	131003	±	11189
1786	132921	±	15441

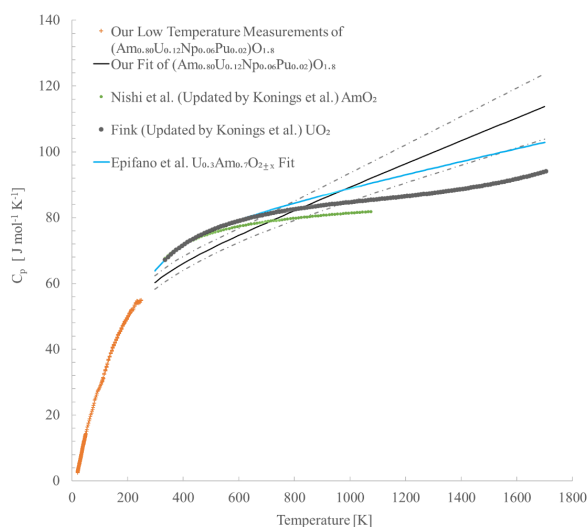


Figure 4. The heat capacity variation with temperature for the $(\text{Am}_{0.80}\text{U}_{0.12}\text{Np}_{0.06}\text{Pu}_{0.02})\text{O}_{1.8}$ determined by fitted Maier–Kelly equation (Equation (4) and Table 2) (solid black line) with the confidence intervals (- . -). Low temperature heat capacity measurements (+) are also included in this graph. Our data compared to the experimentally derived (not extrapolated data) for AmO_2 (green) by Nishi et al. [14], UO_2 (solid grey line) by Fink [32] updated by Konings et al. [33], and $\text{U}_{0.3}\text{Am}_{0.7}\text{O}_{2\pm x}$ by Epifano et al. [17] (blue line). These latter data were constrained by the UO_2 and AmO_2 data, whereas our data are constrained by the low temperature heat capacity data for our material.

Table 2. The linear regression fit parameters for the Maier–Kelly equation (Equation (4)).

Parameter	Value	Uncertainty	Units
a	55.1189	5.681	$\text{J K}^{-1} \text{mol}^{-1}$
b	3.4621×10^{-2}	0.8705×10^{-2}	$\text{J K}^{-2} \text{mol}^{-1}$
c	-4.58312×10^5	1.38792×10^5	J K mol^{-1}

2.3. Discussion

Figure 3 suggests that the measured enthalpy increment data for $(\text{Am}_{0.80}\text{U}_{0.12}\text{Np}_{0.06}\text{Pu}_{0.02})\text{O}_{1.8}$ is consistent with the AmO_2 data by Nishi et al. [19] and its extrapolation, the $\text{U}_{0.3}\text{Am}_{0.7}\text{O}_{2\pm x}$ data recorded under air by Epifano et al. [17] and the various data for UO_2 by Valu et al. [18] and Fink [32]. Figure 3a shows that there is a slight deviation of the $(\text{Am}_{0.80}\text{U}_{0.12}\text{Np}_{0.06}\text{Pu}_{0.02})\text{O}_{1.8}$ data from the extrapolated AmO_2 data [19], e.g. above 1400 K. However, this is also noted for UO_2 dataset by Fink [24]. Figure 3 shows that the uncertainties in the enthalpy increment data generally increased with an increase in temperature in this study. The diverging trend from the $\text{AmO}_{2.00}$ extrapolated data by Nishi et al. [19] was also generally true for the measurements by Epifano et al. [17] of their U-Am oxides with higher americium contents ($\text{Am}/[\text{Am}=\text{U}]$ mol% ratios of 0.49, 0.58 and 0.68) who measured their samples using the same apparatus in air. Indeed, Epifano et al. [17] observed systematically higher enthalpy increment measurements with increasing temperature compared to the extrapolated enthalpy increment–temperature curve for $\text{AmO}_{2.00}$. They explained that this deviation may be due to the AmO_2 reduction to AmO_{2-x} during drop calorimetry, which is expected above 1100 K even under such oxidative conditions. It is, therefore, possible that this slight diverging trend for $(\text{Am}_{0.80}\text{U}_{0.12}\text{Np}_{0.06}\text{Pu}_{0.02})\text{O}_{1.8}$ from the extrapolated $\text{AmO}_{2.00}$ data may be due to the partial reduction of the material. Indeed, in the present study, the measured material is already substoichiometric with an O/M of 1.8 ($M = \text{Am} + \text{U} + \text{Np} + \text{Pu}$), but this ratio may further decrease at high temperature under an argon atmosphere. Overall, the enthalpy increment data for $(\text{Am}_{0.80}\text{U}_{0.12}\text{Np}_{0.06}\text{Pu}_{0.02})\text{O}_{1.8}$ is consistent with data for americium, uranium and mixed americium uranium oxides in the literature, including those for AmO_2 .

Figure 4 illustrates the low and high temperature heat capacity data for $(\text{Am}_{0.80}\text{U}_{0.12}\text{Np}_{0.06}\text{Pu}_{0.02})\text{O}_{1.8}$. The figure also shows that the heat capacity of the new RPS prospect fuel $(\text{Am}_{0.80}\text{U}_{0.12}\text{Np}_{0.06}\text{Pu}_{0.02})\text{O}_{1.8}$ is broadly consistent with the heat capacity temperature variation of AmO_2 , UO_2 and mixed $\text{U}_{0.3}\text{Am}_{0.7}\text{O}_{2\pm x}$ [17]. Therefore, the experimentally determined heat capacity in the present study, or by Epifano et al. [17], show only a minor deviation from pure UO_2 and AmO_2 values. This is despite the highly complex charge distribution in U-Am mixed oxides, especially those with high americium content [34]. To compare the data in greater detail, the heat capacity of $(\text{Am}_{0.80}\text{U}_{0.12}\text{Np}_{0.06}\text{Pu}_{0.02})\text{O}_{1.8}$ is lower than the data for these oxides, e.g. below 600 K. This might be explained by the strong substoichiometry of the material measured in the present study and the presence of oxygen vacancies. It must be noted that values were constrained by Epifano et al. at 298.15 K and considered to be the linear combination of pure UO_2 and AmO_2 for the U-Am mixed oxide data [17]. In this study, with its focus on $(\text{Am}_{0.80}\text{U}_{0.12}\text{Np}_{0.06}\text{Pu}_{0.02})\text{O}_{1.8}$, the fit was obtained together with the experimentally measured low C_p values and is, therefore, free of any assumption. In the case of Epifano et al. [17], their assumption is consistent with their investigation of stoichiometric mixed oxides $(\text{U},\text{Am})\text{O}_{2.00}$. With respect to higher temperature heat capacity data, Figure 4 illustrates that the heat capacity of $(\text{Am}_{0.80}\text{U}_{0.12}\text{Np}_{0.06}\text{Pu}_{0.02})\text{O}_{1.8}$ is greater than that of UO_2 above 1100 K. This might be due to the partial reduction of the material during measurements, as mentioned before [17].

This study determined precise high temperature heat capacity data for this $(\text{Am}_{0.80}\text{U}_{0.12}\text{Np}_{0.06}\text{Pu}_{0.02})\text{O}_{1.8}$ prospect fuel, which will be key for establishing fuel response under high temperature accidents.

Further sintering studies will be conducted in the future. They will provide the opportunity to investigate the effect of grain size on heat capacity. Studies by others [35] note that an increase in grain size can increase heat capacity.

2.4. Heat Capacity Conclusion

The recommended high temperature equation for the heat capacity is

$$C_p(T) = 55.1189 + 3.46216 \times 10^{-2} T - 4.58312 \times 10^5 T^{-2} \quad (5)$$

for temperatures T (in Kelvin) from 293 K to 1786 K. This equation is the result of fitting both low temperature heat capacity data and high temperature enthalpy increment data to the well-known Maier–Kelly equation using a simultaneous least squares linear regression (please see Section 2.1.3). This study provides valuable and essential experimental data for the new European RPS fuel, $(\text{Am}_{0.80}\text{U}_{0.12}\text{Np}_{0.06}\text{Pu}_{0.02})\text{O}_{1.8}$. These enthalpy increment and, in turn, heat capacity data form a vitally important step towards determining the thermal conductivity of the new prospect fuel. The data are broadly consistent with AmO_2 , UO_2 and $\text{U}_{0.3}\text{Am}_{0.7}\text{O}_2$ [17]. The particular heat capacity values, however, do differ, as illustrated in Figure 4. This study has determined data at higher temperatures than those presented in the literature for AmO_2 . Data have, therefore, been recorded for much higher temperatures than for a previous RPS fuel candidate. The investigated temperatures span lower temperatures that will include RPS operational temperatures and high temperatures that could be informative for different design basis accidents. Furthermore, these data contribute to the wider knowledge of the thermal properties of americium-bearing oxides in the literature and, in particular, oxides with high americium content. Future investigations will determine thermal diffusivity of the fuel to determine the thermal conductivity of the fuel and determine its thermal expansion to account for its decreasing density with temperature.

3. Case Study: Estimating Thermal Conductivity of the Fuel and Assessing if Fuel Melting Could Occur When the ELHS Clad is at its Maximum Permitted Temperature (1973 K)

3.1. Purpose

An analytical model will be developed to assess if $(\text{Am}_{0.80}\text{U}_{0.12}\text{Np}_{0.06}\text{Pu}_{0.02})\text{O}_{1.8}$ fuel melting is possible for a hypothetical scenario where the ELHS clad is at the maximum temperature permitted by the RPSs' requirements [12], i.e. 1973 K. The model will determine the maximum temperature of the fuel as a function of clad temperature and fuel thermal conductivity. Estimates for the thermal conductivity of $(\text{Am}_{0.80}\text{U}_{0.12}\text{Np}_{0.06}\text{Pu}_{0.02})\text{O}_{1.8}$ will be made.

The thermal conductivity, k , of a material is defined as the product of its thermal diffusivity, α , density, ρ , and specific heat capacity, c_p , as shown below:

$$k = \alpha \cdot \rho \cdot c_p \quad (6)$$

All of these terms are functions of temperature. The heat capacity, C_p , of $(\text{Am}_{0.80}\text{U}_{0.12}\text{Np}_{0.06}\text{Pu}_{0.02})\text{O}_{1.8}$ was determined as a function of temperature in Section 2. By using the molar mass of the material, which is 269.2 mol g^{-1} according to Vigier et al. [11], these data can be transformed into specific heat capacity, c_p . The theoretical density of the material at room temperature is 10.67 g cm^{-3} [11]. The particular sample investigated for the heat capacity measurements had a relative density of 89% T.D. However, a range of relative densities will be considered here to consider the likely maximum range of possible relative densities that the final sintered RPS fuel forms may have, i.e. 80 to 100% T.D. The effect of different relative densities on the thermal conductivity of a material will be discussed in Section 3.3. For this case study, the known data (described above) and estimates for the thermal diffusivity and thermal expansion of the fuel will be combined to estimate the thermal conductivity of the fuel.

The specific objectives of this part of this study are to:

1. Develop an analytical thermal model to describe the maximum temperature of the fuel as a function of the fuel thermal conductivity, the outer surface temperature of the fuel, and the inner surface temperature of the clad. This will consider the effect of radiation-only and conduction-only between the fuel and clad to estimate an envelope of maximum fuel temperatures for a given clad temperature. Curves of the maximum fuel temperature as a function of fuel thermal conductivity will be estimated for a clad inner surface temperature, $T_{i, cl}$, (1) at 623 K that represents the RTG's standard operation and (2) (i) at 1750 K, which is slightly lower than the approximate maximum temperature for which heat capacity data were determined and (ii) at 1900 K and (iii) 1973 K. Temperatures (i) and (ii) are included informatively to provide additional data for high clad temperatures.
2. Compare the maximum fuel temperature determined using the long-standing University of Leicester RTG finite element thermal model to the results of the analytical thermal model to assess the confidence in the analytical thermal model. Specifically, it will be assessed if the FE thermal model that considers both radiation and conduction between the fuel and the clad provides a maximum fuel temperature solution that lies within the envelope predicted by the analytical thermal model.
3. Estimate the thermal conductivity of $(Am_{0.80}U_{0.12}Np_{0.06}Pu_{0.02})O_{1.8}$ as a function of temperature using the experimental heat capacity data of this paper (Section 2), the known theoretical and relative density of the fuel (80–100% T.D.), assumptions for the thermal diffusivity of different americium/uranium oxides, and an assumption for its thermal expansion based on one of these oxides. Upper and lower limits of thermal diffusivity will be used to provide a range in thermal conductivity values. This will allow a range in potential maximum fuel temperatures for the RTG/ELHS to be seen. Lower estimates of the fuel conductivity at a given temperature will be made using the lower confidence interval data for the heat capacity values (shown in Figure 4) and the lowest thermal diffusivity data. These will be used for objectives 4–6 below.
4. Estimate a range of values for the maximum fuel temperature of the RTG during its standard operation (623 K inner clad temperature) based on the thermal conductivity estimates.
5. Assess the maximum fuel temperature curves generated by the analytical thermal model for 1750 K, 1900 K and 1973 K clad temperatures to estimate the maximum fuel temperature of the ELHS using the lowest thermal conductivity estimates for an 80% T.D. fuel. Specifically, it will be assessed whether fuel melting is possible (assumptions for this will be made based on the lowest melting temperature of americium/uranium oxides in the literature).
6. Review the outcomes with respect to RPS safety and whether recommendations for the future fuel R&D are required.

3.2. Theory: Analytical Thermal Model for RTG/ELHS Maximum Fuel Temperature

A recent design of the European RTG/ELHS with its twelve fuelled Pt-20%Rh clads is shown in Figure 1. The RTG/ELHS system operates under a constant power regime where the thermal power is provided by the $(Am_{0.80}U_{0.12}Np_{0.06}Pu_{0.02})O_{1.8}$ fuel totalling 200 W_{th} (The term 'thermal power' is used here to distinguish this power from the resultant electrical power that the RTG generates.). The outer surface temperature of a clad and the inner surface temperature of the clad are constant under a given scenario of RTG/ELHS operation. This is due to the constant power regime of the RTG/ELHS (and RHU) system. More so, the temperatures of the clad are dictated by the temperatures external to the RTG/ELHS. For example, the external temperature and the thermal properties of the RTG components dictate the temperatures across the RTG's radiator fins and of all the RTG's consecutive inner layers (subsystems) and, therefore, of the clad.

The analytical thermal model considers heat transfer between a single clad and the fuel inside. The RPS programme has not concluded whether the fuel in a given clad will comprise a single high aspect ratio pellet or a stack of low aspect ratio discs of equivalent

total volume (the latter is more likely). Here, the analytical model assumes the fuel to be a single cylinder with a volume equal to the pellet.

The maximum temperature of the fuel, T_{max} , will occur at the centre of the fuel cylinder (see Appendix B). The equation for T_{max} of the RTG has been derived and is a function of the outer surface temperature of the fuel in the radial direction, T_s , and of the thermal conductivity of the fuel, k . T_s is then a function of the clad temperature, which will be described shortly. The reader is referred to Appendix B of this article for details of the T_{max} derivation. The equation is:

$$T_{max} = T_s + \frac{\dot{q}l^2}{2k} \left[1 + \sum_{n=1}^{\infty} \frac{4(-1)^n}{\lambda_n^3 l^3 I_0(\lambda_n a)} \right] \quad (7a)$$

where \dot{q} is the power per unit volume of the fuel, i.e. $831,693 \text{ W m}^{-3}$, in this case, as a single RTG that produces 10 W of electrical power comprises 12 fuelled clads providing a total of 200 W_{th} . Each clad contains $2.00 \times 10^{-5} \text{ m}^3$ of fuel. Additionally, $2l$ is the height of the fuel in a clad, k is the thermal conductivity of the fuel, a is the radius of the fuel and λ_n describe constants defined by

$$\lambda_n = \frac{1}{2l}(2n - 1)\pi, n = 1, 2, \dots \quad (7b)$$

and I_0 is a modified Bessel function of the first order. Again, the reader is referred to Appendix B for a detailed explanation of these parameters. For the RTG, $2l$ is equal to 0.035 m (3.5 cm) and the radius is equal to 0.0135 m (1.35 cm).

The value of T_s is dictated by the heat transfer route between the fuel and the clad. For the case of conduction, the outer surface of the fuel and inner surface of the clad are in contact, i.e.

$$T_s = T_{i\ cl} \quad (7c)$$

For the case of radiation-only between the fuel and the clad:

$$T_s = \left(\frac{Q}{A\sigma\epsilon_{eff}} + T_{i\ cl}^4 \right)^{\frac{1}{4}} \quad (7d)$$

where Q is the thermal power production of a single pellet, i.e. 16.67 W_{th} , A is the surface area of the fuel pellet, σ is the Stefan–Boltzmann constant, and, finally, ϵ_{eff} is the effective emissivity of the fuel and clad. For any small enough area between the fuel and the clad, the fuel's outer surface and the clad's inner surface can be assumed to be equivalent to two parallel layers, such that ϵ_{eff} is defined as

$$\epsilon_{eff} = \frac{1}{\frac{1}{\epsilon_s} + \frac{1}{\epsilon_{i\ cl}} - 1} \quad (7e)$$

where ϵ_s is the emissivity of the surface of the fuel and $\epsilon_{i\ cl}$ is the emissivity of the inner surface of the clad, i.e. of Pt-20%Rh. The emissivity of the fuel is assumed to be 0.83, which was the value assumed for U-Am mixed oxides [36], UO_2 and PuO_2 in the literature [37,38]. As the emissivity of Pt is much lower than U-Am oxide, the effective emissivity will be dominated by the assumption for the clad. This finding is beneficial as it reduces the effect of the uncertainty of an unknown emissivity of the fuel.

All three RPSs have Pt-20%Rh clads. The emissivity of the Pt-20%Rh and its variation with temperature could not be readily located in the literature. Data for Rh exists [39,40] but data at lower temperatures were not located. Under standard RTG operating conditions, $T_{i\ cl}$ is 623 K . With reference to the range of $T_{i\ cl}$ values in this study, data exist for pure Pt and Pt-10%Rh [41–44], which is assumed to be approximately representative of Pt-20%Rh. The literature suggests that data for Pt should be “representative of platinum alloys” [45].

Only a limited data set could be sourced for lower temperatures [41,42] and only data for Pt could be sourced for around 623 K [41,44]. The latter reference reviewed data from a number of studies that suggested the emissivity could range between 0.07 and 0.14 with most data suggesting a value below 0.1. The former reference [41] suggested that the emissivity could range between 0.06 and 0.07. To be conservative, a value of 0.06 latter is assumed as this would result in a larger estimate for the maximum fuel temperature in a radiation-only regime. This therefore envelopes a greater range of temperatures, which will encompass those predicted by the higher emissivity values.

Finally, an estimate for the emissivity of Pt-20%Rh at 1973 K is required. The emissivity of Pt or PtRh alloys at this temperature could not be located. Foote [41] suggests that the emissivity of Pt could range between 0.175 and 0.18 at 1973 K. However, a more modern source [43] suggests that the emissivity of Pt could be 0.18 for a wire sample at 1673 K and 0.191 for an unoxidised sample at 1773 K. Here, an emissivity of 0.2 is assumed for 1973 K. This may represent a lower estimate for the emissivity of Pt-20%Rh at 1973 K given that a higher emissivity value (~ 0.22) was estimated for Pt-10%Rh at 1723 K [42].

3.2.1. The Fuel Temperature Difference, $T_{max} - T_s$, Relationship

A general curve for $T_{max} - T_s$ against the fuel thermal conductivity, K , is shown in Figure 5. The former was determined using a rearranged form of Equation (7a). The temperature difference is independent of the clad's inner surface temperature. It is, therefore, independent of whether the RTG is in an operation or accident scenario. Figure 5 illustrates how $T_{max} - T_s$ increases with an increasing gradient as the fuel thermal conductivity reduces, particularly, below $1 \text{ W m}^{-1} \text{ K}^{-1}$. The gradient increases most significantly when the thermal conductivity is below around $0.5 \text{ W m}^{-1} \text{ K}^{-1}$.

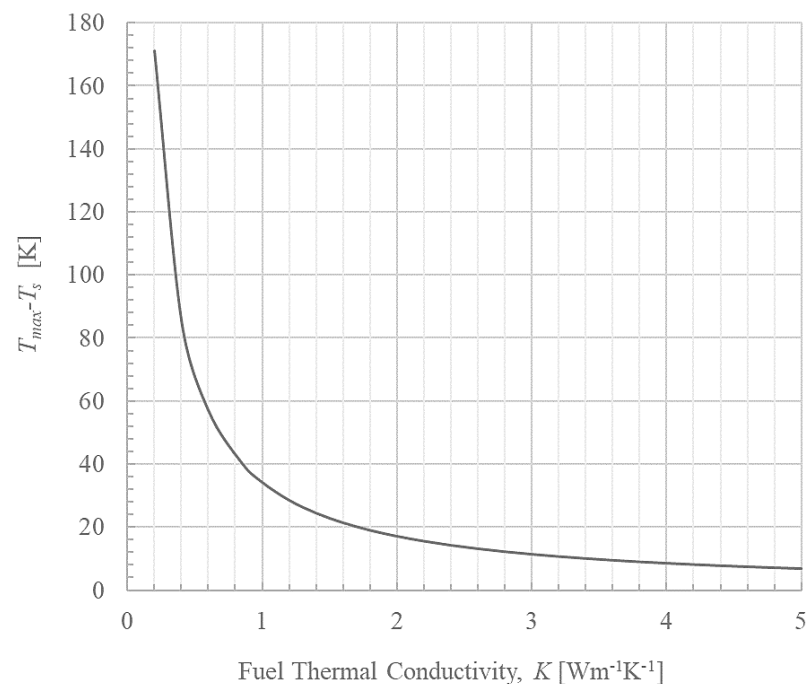


Figure 5. The $T_{max} - T_s$ variation as a function of fuel thermal conductivity, K .

Figure 5 can be used to easily estimate the maximum fuel temperature for the RTG/ELHS in a conduction-only regime by assuming that T_s is equal to the clad temperature (c.f. Equation (7a,c)). T_s needs to be known to estimate the maximum fuel temperature, i.e. the clad temperature needs to be known. Radiation between the fuel and clad needs to be considered (c.f. Equation (7d)) to determine the greatest maximum fuel temperature for a given fuel thermal conductivity (A subtle point is noted: the temperature of the fuel varies radially, and the thermal conductivity of the fuel is a function of

temperature. The analysis from this point onwards assumes an effective averaged thermal conductivity value as the temperature gradient across the fuel is small). This will result in a T_s larger than $T_{i\ cl}$. Equation (7a) can, therefore, be used to produce two curves for the maximum fuel temperature in the form of upper and lower estimates as a function of fuel thermal conductivity based on radiation-only and conduction-only regimes, respectively. An example of this will be presented in Section 3.2.2.

3.2.2. Maximum Fuel Temperature Results Comparison between Analytical Thermal Model and RTG FE Thermal Model (RTG under Standard Operation)

In order to estimate T_{max} for the RTG under standard operating conditions as a function of fuel thermal conductivity, Equation (7a) is plotted assuming a clad inner temperature, $T_{i\ cl}$ of 623 K. This is shown in Figure 6. It illustrates that the route of coupling (radiation or conduction) between the fuel and the clad has a large effect on the maximum fuel temperature for the RTG (under standard operating conditions) regardless of the fuel thermal conductivity. In practice, the heat transfer between the fuel and the clad will be a combination of the two heat transfer routes. Therefore, the maximum fuel temperature will lie between the illustrated conduction-only and radiation-only curves in Figure 6.

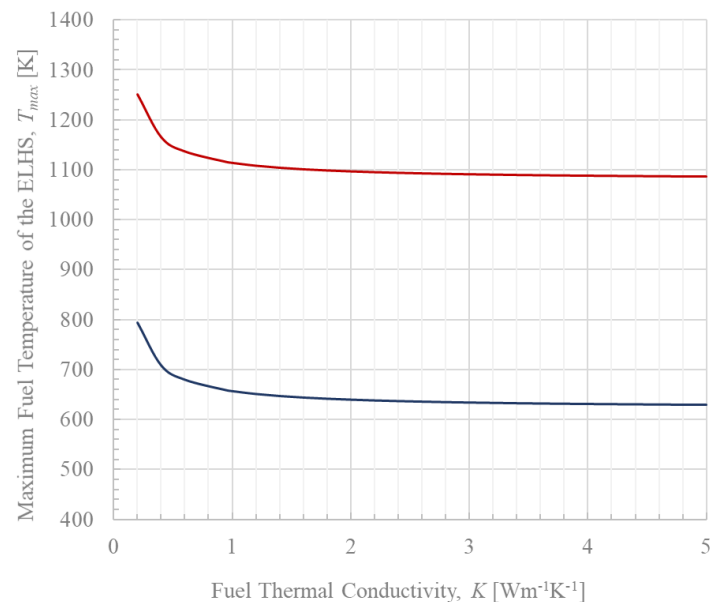


Figure 6. The maximum fuel temperature in the RTG as a function of fuel thermal conductivity under standard operational conditions (clad temperature of 623 K) under conduction-only (blue) and radiation-only (red) heat transfer between the fuel and clad.

An example fuel thermal conductivity is now considered to see if the analytical model produces a result that is consistent with the long-standing FE model for the RTG under standard operational conditions. The thermal conductivity of 100% T.D. AmO_{2-x} established by Nishi et al. as a function of temperature [46,47] is inputted into the FE model for the recent RTG. This material has been assumed for past RTG FE thermal models. The arrived maximum fuel temperature solution is 415 °C, i.e. 688 K, as shown in Figure 7. According to the data by Nishi et al., this corresponds to an approximate thermal conductivity between 2 and 2.3 $\text{W m}^{-1} \text{K}^{-1}$ [46,47]. According to Figure 6, the analytical model suggests that the maximum RTG fuel temperature under standard operation for a 2 $\text{W m}^{-1} \text{K}^{-1}$ fuel thermal conductivity would be between 640 K for a conduction-only regime and about 1095 K for the radiation-only case. The result of the FE model, which considers conduction through the fuel's upper and lower surfaces to the clad, and radial radiation to the clad's walls, therefore, lies within these limits. This comparison, therefore,

provides confidence in the analytical thermal model. However, the greatest value of this analytical thermal model is in understanding the maximum temperature of the fuel for the ELHS under extreme clad temperatures.

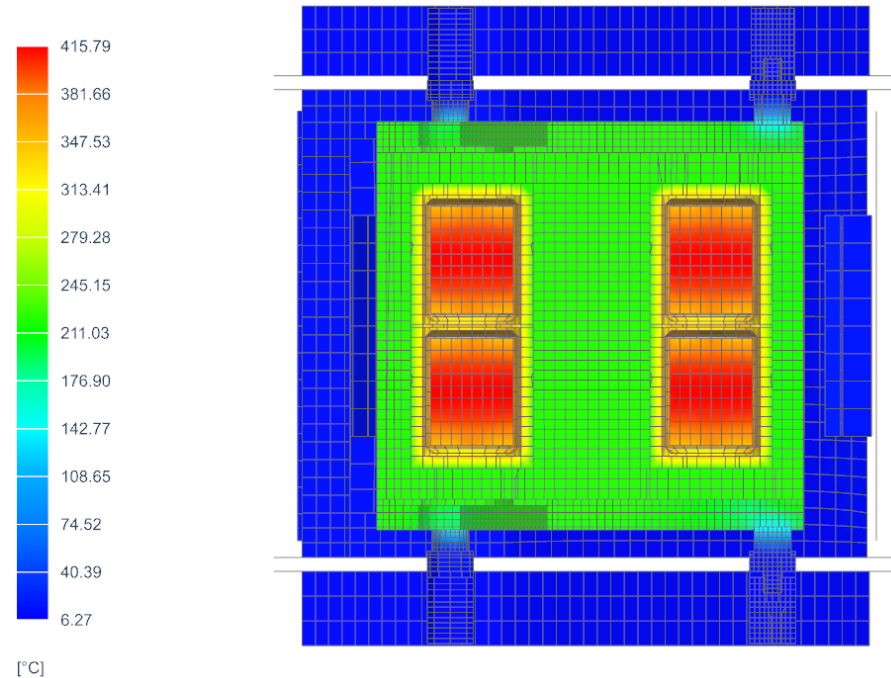


Figure 7. The temperature distribution of the RTG determined by the University of Leicester FM model for its standard operation. A thermal conductivity function of 100% T.D AmO_{2-x} is based on data by Nishi et al. [46,47]. A Pt-20%Rh emissivity of 0.06 is assumed here.

3.3. Thermal Conductivity Estimates

Equation (6) showed how the thermal conductivity of a material is a product of the density, thermal diffusivity and specific heat capacity of a material where each is a function of temperature. Figure 4 illustrates how the heat capacity of $(\text{Am}_{0.80}\text{U}_{0.12}\text{Np}_{0.06}\text{Pu}_{0.02})\text{O}_{1.8}$ is consistent yet different to AmO_2 , UO_2 and $\text{U}_{0.3}\text{Am}_{0.7}\text{O}_{2\pm x}$ [17]. Additionally, the theoretical density of $(\text{Am}_{0.80}\text{U}_{0.12}\text{Np}_{0.06}\text{Pu}_{0.02})\text{O}_{1.8}$ (10.67 g cm^{-3} [11]) differs to that of UO_2 (10.963 g cm^{-3} [32]), and AmO_2 (11.67 g cm^{-3} [32]). It is, therefore, not unreasonable to assume that the thermal conductivity of $(\text{Am}_{0.80}\text{U}_{0.12}\text{Np}_{0.06}\text{Pu}_{0.02})\text{O}_{1.8}$ may differ to UO_2 , AmO_2 or AmO_{2-x} (it will have a lower density than AmO_2) even if, hypothetically, its thermal diffusivity as a function of temperature is very close to these oxides.

The thermal diffusivities of different cubic/multiple cubic phased americium oxides, uranium oxide or mixed americium uranium oxides in the literature were reviewed, specifically AmO_2 [19], UO_2 [32], AmO_{2-x} [46,47] and $(\text{U}_{1-y}, \text{Am}_y)\text{O}_{2-x}$ solid solutions with y equal to 0.0877 and 0.1895 [18]. The latter, which were developed by Valu et al., are simply denoted by Am10 Am20 for ease [18]. Nishi et al. recorded data for AmO_2 up to around 1100 K [19] (presumably because it reduces above this temperature). The thermal diffusivity data for AmO_2 is not considered further for estimating the thermal conductivity of $(\text{Am}_{0.80}\text{U}_{0.12}\text{Np}_{0.06}\text{Pu}_{0.02})\text{O}_{1.8}$ as temperatures beyond 1100 K will be explored. Data exist for all of the other oxides between around 550 K and 1550 K [18,32,46,47] and data for UO_2 were recorded up to at least 2800 K by Vlahovic et al. [48]. Within the aforementioned temperature range, UO_2 had the greatest thermal diffusivity and AmO_{2-x} had the lowest values.

Equation (6) is used to estimate the thermal conductivity of $(\text{Am}_{0.80}\text{U}_{0.12}\text{Np}_{0.06}\text{Pu}_{0.02})\text{O}_{1.8}$ at different temperatures. Specifically, the (specific) heat capacity data determined in this study (Section 2), the known theoretical density [11], and thermal diffusivity values of UO_2 based on the study by Vlahovic et al. [48], and of AmO_{2-x} based on the study by Nishi

et al. are used [46,47]. The values used are noted in Table 3. The different assumptions for the thermal diffusivity as a function of temperature are used to estimate a range of potential thermal conductivities for a given temperature. Data based on AmO_{2-x} allow a lower estimate to be made, given that AmO_{2-x} has the lowest thermal diffusivity of the various considered oxides in the literature (as noted in the previous paragraph). The UO_2 thermal diffusivity data allow a higher estimate for the thermal conductivity to be made, which is informative. The lowest thermal conductivity estimates are considered here because they will cause greatest maximum fuel temperatures of the RTG/ELHS. If such a thermal conductivity does not cause a fuel melting temperature to be reached, then a higher thermal conductivity will not result in fuel melting. It is noted that Nishi et al. [46,47] only presented their AmO_{2-x} thermal diffusivity data in plotted form and did not provide a line of best fit. To aid the estimation of their AmO_{2-x} thermal diffusivity data [46] at different temperatures, the raw data values were estimated and extracted from their graph using WebplotDigitizer [49]. These are shown in Figure A3 in Appendix C. The illustrated power law function provided the best fit (conducted in MS Excel). Its equation is reported in Appendix C.

An assumption is made for the thermal expansion of $(\text{Am}_{0.80}\text{U}_{0.12}\text{Np}_{0.06}\text{Pu}_{0.02})\text{O}_{1.8}$ to account for the reduction in density and, therefore, thermal conductivity with temperature. No known data exist for macroscopic length expansion or bulk volume expansion of americium oxides and mixed americium uranium oxides. Only lattice parameter or lattice volume expansion data exist, e.g., for AmO_2 by Lebreton et al. [50] or for $\text{U}_{0.33}\text{Am}_{0.67}\text{O}_{2\pm x}$ by Epifano et al. [51]. It is not uncommon to consider lattice parameter measurements to indicate the bulk expansion of materials, as noted by a review by Fink [32] for UO_2 . Here, as an estimate, $(\text{Am}_{0.80}\text{U}_{0.12}\text{Np}_{0.06}\text{Pu}_{0.02})\text{O}_{1.8}$ is assumed to have a bulk volume expansion equal to the lattice volume expansion of $\text{U}_{0.33}\text{Am}_{0.67}\text{O}_{2\pm x}$ [51]. The latter material is a cubic oxide [51]. It has the greatest americium metal fraction of the mixed uranium americium oxides with lattice expansion data in the literature. In order to estimate the volume expansion, the lattice parameter relationship developed by Epifano et al. [51] for $\text{U}_{0.33}\text{Am}_{0.67}\text{O}_{2\pm x}$ as a function of temperature, $a(T)$, is first normalised relative to its room temperature lattice parameter, a_{RT} , to give:

$$\frac{a(T)}{a_{RT}} = 1 + (1.197 \times 10^{-5}(T - 298.15)), \quad (8)$$

where T is the temperature in Kelvin and 298.15 refers to room temperature. Then, the cube of Equation (8) gives the lattice volume expansion of this cubic material. For the reader's reference, the volume expansion is broadly similar to—yet slightly greater than—the volume expansion of UO_2 [32]. This relationship is assumed as a first estimate for the bulk volume expansion of $(\text{Am}_{0.80}\text{U}_{0.12}\text{Np}_{0.06}\text{Pu}_{0.02})\text{O}_{1.8}$. The use of linear expansion data to estimate the decrease in density of a material with temperature has been demonstrated in the literature, e.g. by Fink for UO_2 [32]. In a similar way, the decrease in density of $(\text{Am}_{0.80}\text{U}_{0.12}\text{Np}_{0.06}\text{Pu}_{0.02})\text{O}_{1.8}$ with temperature is assumed to follow:

$$\rho(T) = \rho_{RT} \frac{V}{\Delta V} = \rho_{RT} \left(1 + (1.197 \times 10^{-5})\right)^{-3} \quad (9)$$

where ρ_{RT} is the 100% T.D. of the fuel. This is 10.67 g cm^{-3} according to Vigier et al. [11].

Equation (6) is used to estimate the thermal conductivity of 100% T.D. $(\text{Am}_{0.80}\text{U}_{0.12}\text{Np}_{0.06}\text{Pu}_{0.02})\text{O}_{1.8}$ at a given temperature using a density estimate from Equation (9), the heat capacity (Equation (5) transformed to specific heat using the molar mass of the material, 269.2 mol g^{-1} [11]) and an assumption for the thermal diffusivity data.

A relative density of less than 100% T.D. decreases the thermal conductivity of a material. The thermal conductivity (at a given temperature) of the sintered $(\text{Am}_{0.80}\text{U}_{0.12}\text{Np}_{0.06}\text{Pu}_{0.02})\text{O}_{1.8}$ with a particular relative density is then estimated using the following equation by Schulz [52]:

$$k = k_{T.D.} (1 - P)^x \quad (10)$$

where $k_{T,D}$ is the thermal conductivity at a given temperature at 100% T.D. (c.f. Equation (6)), P is the porosity of the sample such that $1 - P$ is the relative density of the sample, and x is a constant to be defined. This equation was used by Nishi et al. [46] to describe the effect of different porosities and, therefore, relative densities on the thermal conductivity of AmO_{2-x} . They state this was valid for porosities up to 0.3 (relative densities as low as 70% T.D.). They assumed x equalled 1.5. The same x value is assumed here.

The values used/assumed for the parameters in Equation (6) are presented in Table 3. Their references are provided for full visibility. Further still, the lower confidence interval heat capacity values are also shown to allow an even lower estimate of the thermal conductivity of the $(\text{Am}_{0.80}\text{U}_{0.12}\text{Np}_{0.06}\text{Pu}_{0.02})\text{O}_{1.8}$ material to be made (using the AmO_{2-x} thermal diffusivity data). Figure 8 illustrates selected thermal conductivity estimates, namely those based on UO_2 thermal diffusivity data, and those based on AmO_{2-x} thermal diffusivity data and the heat capacity lower confidence interval data for $(\text{Am}_{0.80}\text{U}_{0.12}\text{Np}_{0.06}\text{Pu}_{0.02})\text{O}_{1.8}$. The ‘error’ bars here do not indicate error but instead are used to represent the 100% T.D. (top bar) and 80% T.D. (bottom bar) thermal conductivity estimates that cover the maximum likely range for the RPS fuel densities considered during fuel R&D.

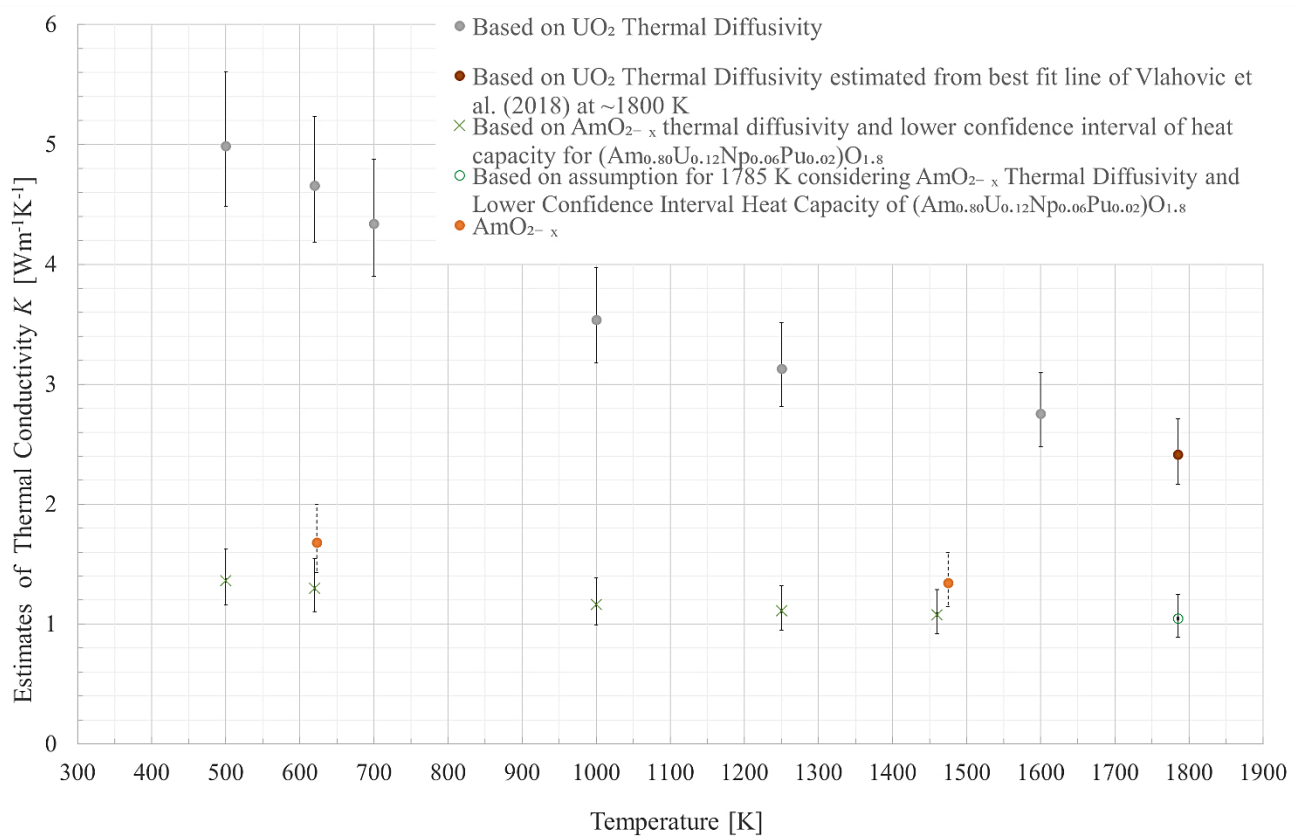


Figure 8. Examples of thermal conductivity estimates for $(\text{Am}_{0.80}\text{U}_{0.12}\text{Np}_{0.06}\text{Pu}_{0.02})\text{O}_{1.8}$ with 89% T.D. (the plotted points) from Table 3. The thermal diffusivity assumptions were based on UO_2 or AmO_{2-x} . For the latter, the plotted points were based on lower confidence interval of the heat capacity data for $(\text{Am}_{0.80}\text{U}_{0.12}\text{Np}_{0.06}\text{Pu}_{0.02})\text{O}_{1.8}$ to estimate a lower thermal conductivity. The ‘error’ bars here do not indicate errors but instead are used to represent the 100% T.D. (top bar) and 80% T.D. (bottom bar) thermal conductivities that cover the maximum likely range for the RPS fuel. An estimate (data legend: o) based on extrapolation of the AmO_{2-x} thermal diffusivity data of Nishi et al. [46] was used to estimate a possible thermal conductivity at 1785 K. Data for AmO_{2-x} at 80–100% T.D. are plotted and were based on the data by Nishi et al. for 100% T.D. The orange points represent an 89% T.D.

Table 3. The assumptions and experimental data used to estimate thermal conductivity values for the $(Am_{0.80}U_{0.12}Np_{0.06}Pu_{0.02})O_{1.8}$ assuming different thermal diffusivity values. The lower confidence interval value of the heat capacity, C_p , is also considered for lower estimates. Different relative densities are also assumed to establish the range of thermal conductivities that a sintered $(Am_{0.80}U_{0.12}Np_{0.06}Pu_{0.02})O_{1.8}$ fuel may have.

$(Am_{0.80}U_{0.12}Np_{0.06}Pu_{0.02})O_{1.8}$						α Assumed Data		Thermal Conductivity Estimates ($Wm^{-1} K^{-1}$) at:						
T (K)	T.D. ($g\ cm^{-3}$)	Assum. Vol. Expansion% (Equation (9))	Assum. T.D. at T (kgm^{-3})	C_p (Equation (5)) ($J\ mol^{-1}K^{-1}$)	Lower C_p Confid. Interv. ($J\ mol^{-1}K^{-1}$)	Mol. Mass ($molg^{-1}$)	Oxide Used to Assume α	Ref.	$\alpha \times 10^{-6}$ (m^2s^{-1})	100% T.D.	95% T.D.	89% T.D.	85% T.D.	80% T.D.
500	10.67 [11]	1.007	10593	70.596		269.2 [11]	UO_2	Vlahovic et al. [48] raw data at 499 K	2.02	5.6	5.3	5.0	4.8	4.5
620		1.012	10548	75.392				1.77	5.2	5.0	4.7	4.4	4.2	
700		1.014	10518	78.419				1.59	4.9	4.6	4.3	4.1	3.9	
1000		1.025	10406	89.282				1.15	4.0	3.8	3.5	3.4	3.2	
1250		1.035	10313	98.102				0.936	3.5	3.3	3.1	3.0	2.8	
1600		1.047	10186	110.34				0.742	3.1	2.9	2.8	2.6	2.5	
1600		1.047	10186	110.33				0.702	2.9	2.8	2.6	2.5	2.3	
1785		1.054	10120	116.77				0.620	2.7	2.6	2.4	2.3	2.2	
500		10.67 [11]	1.007	10593	70.596				269.2 [11]	AmO_{2-x}	Power Law fit of Nishi et al. [46] data (Equation (A38) in Appendix C)	0.602	1.67	1.55
500	1.007		10593		68.518	0.602	1.62	1.50			1.36	1.27	1.16	
620	1.012		10548	75.392		0.539	1.59	1.47			1.34	1.25	1.14	
620	1.012		10548		73.188	0.539	1.55	1.43			1.30	1.21	1.11	
1000	1.025		10406	89.282		0.421	1.45	1.35			1.22	1.14	1.04	
1000	1.025		10406		84.999	0.421	1.38	1.28			1.16	1.09	0.99	
1250	1.035		10313		91.892	0.376	1.32	1.22			1.11	1.04	0.95	
1460	1.042		10237	105.45		0.347	1.39	1.29			1.17	1.09	1.00	
1460	1.042		10237		97.528	0.347	1.29	1.19			1.08	1.01	0.92	
1785	1.054		10120	116.77		0.313	1.37	1.27			1.15	1.08	0.98	
1785	1.054	10120		106.13	0.313	1.25	1.16	1.05	0.98	0.89				

The maximum temperature at which the thermal diffusivity of AmO_{2-x} was recorded by Nishi et al. [46] was about 1475 K. This temperature was estimated from their plotted results (results were not tabulated). The gradient of their thermal diffusivity became shallower and began to plateau as the temperature tended towards this temperature. To provide a first estimate of the thermal conductivity of the fuel at higher temperatures using these data, an assumption of AmO_{2-x} thermal diffusivity beyond 1475 K was made, which could be valid at 1785 K. This is the approximate upper temperature limit for which $(\text{Am}_{0.80}\text{U}_{0.12}\text{Np}_{0.06}\text{Pu}_{0.02})\text{O}_{1.8}$ heat capacity data were determined in this study. The thermal diffusivity was estimated, using the power law best fit noted in Appendix C (Equation (A38)), to be $3.13 \times 10^{-7} \text{ m}^2\text{s}^{-1}$. This is shown in the Table 3. Although there will be uncertainty in this estimate, the very shallow gradient of the AmO_{2-x} thermal diffusivity curve [46] towards 1475 K is assumed to continue beyond this temperature, e.g. up to 2000 K. The thermal diffusivity at 1973 K could be $2.97 \times 10^{-7} \text{ m}^2 \text{ s}^{-1}$ according to Equation (A38). These estimated thermal diffusivities are noted in Table 3.

The plotted thermal conductivity data of 100% T.D. AmO_{2-x} by Nishi et al. [46] were observed and estimated to be about $2 \text{ Wm}^{-1}\text{K}^{-1}$ and $1.6 \text{ Wm}^{-1}\text{K}^{-1}$ at around 625 K and 1475 K, respectively (based on the lowest values plotted in Nishi et al. at a given temperature). Thermal conductivities of 89% T.D. and 80% T.D. AmO_{2-x} at these temperatures were estimated using Equation (10). These are plotted in Figure 8 to enable comparison with the mixed oxide. The central value represents the 89% T.D. value and the bottom and top of the 'error' bars represent the 80% T.D. and 100% T.D., respectively.

In order to estimate the effect of the ELHS clad being at 1973 K on the maximum fuel temperature, estimates of the fuel's thermal conductivity above 1785 K need to be made. The lowest thermal conductivity estimates are most key to this study because they will result in higher maximum fuel temperatures. The thermal conductivity curve based on AmO_{2-x} thermal diffusivity data is, therefore, considered. The lowest thermal conductivity at 1785 K was estimated to be $0.89 \text{ Wm}^{-1}\text{K}^{-1}$, as shown in Table 3 and Figure 8. The figure shows that as the temperature increases, the gradient of the curve becomes shallower. It is, therefore, assumed that a thermal conductivity between $0.85 \text{ Wm}^{-1}\text{K}^{-1}$ and $0.89 \text{ Wm}^{-1}\text{K}^{-1}$ could be used for the thermal conductivity of the 80% T.D. fuel at slightly higher temperatures, though the limit is unclear. To be conservative, a thermal conductivity estimate of $0.85 \text{ Wm}^{-1}\text{K}^{-1}$ for an 80% T.D. fuel is considered for a temperature at 1900 K based on Figure 8. If it is too low an estimate, it allows the possibility of higher maximum fuel temperatures to be considered for thermal conductivities between $0.85 \text{ Wm}^{-1}\text{K}^{-1}$ and $0.89 \text{ Wm}^{-1}\text{K}^{-1}$. This is particularly important as the possibility of fuel melting is being considered in this study. Finally, it is assumed that the thermal conductivity of a fuel at temperatures greater than 1973 K (the maximum permitted $T_{i \text{ cl}}$ by the RPS requirements) could be as low as $0.8 \text{ Wm}^{-1}\text{K}^{-1}$ as a conservative estimate.

3.4. Results

3.4.1. Maximum Fuel Temperature in RTG under Standard Operation

Figure 6 shows the variation of the maximum fuel temperature with fuel thermal conductivity for the RTG under standard operation, i.e. for a clad inner surface temperature of 623 K. It illustrates that the maximum fuel temperature could be up to 1250 K. The temperature range will be constrained further in Section 4 in the Discussion section.

3.4.2. Maximum Fuel Temperature in ELHS with a Clad Temperature at its Maximum Permitted Limit

A thermal conductivity estimate was made for the fuel at 1785 K. A slightly lower clad temperature was considered initially, i.e. 1750 K. The variation of the maximum fuel temperature of the ELHS as a function of fuel conductivity is shown in Figure 9 for three clad temperatures: 1750 K, 1900 K and 1973. The latter is the maximum permitted temperature of the clad according to requirements [12], and the 1900 K temperature allows an

interim temperature to be considered. The lowest estimate of the fuel thermal conductivity is plotted as the dashed line in each graph in Figure 9.

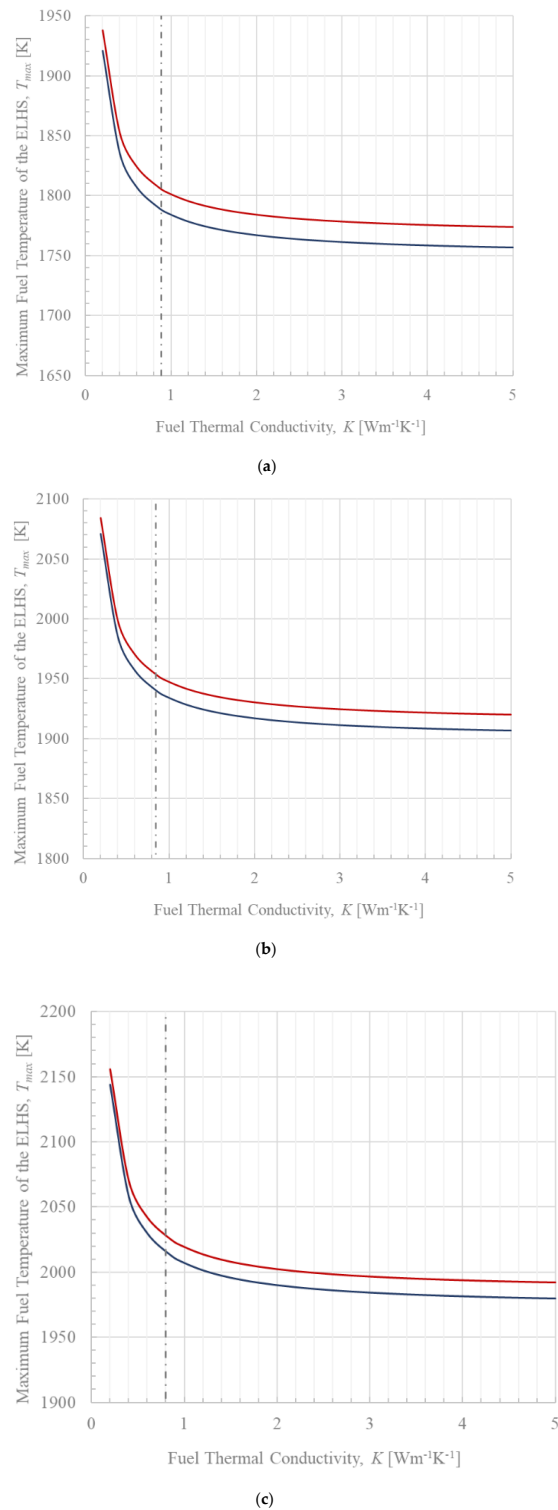


Figure 9. T_{max} as a function of fuel thermal conductivity, K , for a clad inner surface temperature, $T_{i,cl}$ of (a) 1750 K, (b) 1900 K and (c) 1973 K under conduction-only (blue) and radiation-only (red) heat transfer between the fuel and clad. The dashed lines are the lower thermal conductivity estimates for $(Am_{0.80}U_{0.12}Np_{0.06}Pu_{0.02})O_{1.8}$.

4. Discussion

4.1. Maximum Fuel Temperature in RTG under Standard Operation

Constraints for the thermal conductivity values are now considered to constrain the estimated range for the maximum fuel temperature. Firstly, by definition, the internal parts of the fuel (i.e. not at the surface) will have a temperature greater than that of the inner surface of the clad, i.e. greater than 623 K. This is the case for both conduction-only and radiation-only regimes between the fuel and clad. Figure 8 shows that at around this temperature, the 100% T.D. thermal conductivity estimate based on UO_2 thermal diffusivity is about $5.2 \text{ Wm}^{-1}\text{K}^{-1}$ or about $4.2 \text{ Wm}^{-1}\text{K}^{-1}$ for an 80% T.D. fuel. The latter corresponds to a minimum fuel temperature of around 630 K in a conduction-only regime and a maximum temperature of around 1090 K in a radiation-only regime according to Figure 6. In fact, these temperatures (for each regime) are approximately the same for a fuel thermal conductivity of $5.2 \text{ Wm}^{-1}\text{K}^{-1}$ as $4.2 \text{ Wm}^{-1}\text{K}^{-1}$, which is consistent with the plateaus of Figure 6 with increasing thermal conductivity. Figure 6 also illustrates that the maximum fuel temperature under a radiation-only regime would be around 1250 K for a fuel thermal conductivity of $0.2 \text{ Wm}^{-1}\text{K}^{-1}$. As an actinide oxide, it is extremely unlikely that the 100% T.D. fuel would have a thermal conductivity as low as this. It is, therefore, unrealistic for an 80% T.D. fuel. The lowest fuel thermal conductivity estimate at 1250 K was around $0.95 \text{ Wm}^{-1}\text{K}^{-1}$ according to Table 3 and Figure 8 (based on 80% T.D. and the lower confidence interval heat capacity data). The fuel's thermal conductivity will be greater than $0.95 \text{ Wm}^{-1}\text{K}^{-1}$ if the limiting temperature of the fuel is 1250 K according to Figure 8. The majority of the fuel will be less than this temperature. According to Figure 6, a fuel thermal conductivity of $0.95 \text{ Wm}^{-1}\text{K}^{-1}$ would imply a maximum fuel temperature of around 660 K in a conduction-only regime or slightly less than 1120 K (rounded to three significant figures) in a radiation-only regime. This study therefore estimates that the fuel temperature of the RTG during its standard operation could be between 630 K and 1120 K. The maximum fuel temperature will likely be lower than 1120 K as the fuel thermal conductivity would likely be greater than $0.95 \text{ Wm}^{-1}\text{K}^{-1}$.

4.2. Maximum Fuel Temperature in ELHS with a Clad Temperature at its Maximum Permitted Limit

It is firstly noted that the lowest estimates for the thermal conductivity of $(\text{Am}_{0.80}\text{U}_{0.12}\text{Np}_{0.06}\text{Pu}_{0.02})\text{O}_{1.8}$ based on the AmO_{2-x} thermal diffusivity data are similar yet slightly lower than those of the thermal conductivity of AmO_{2-x} . This can be seen by comparing some example temperatures at around 620 K and 1475 K in Figure 8. The latter is around the maximum temperature that Nishi et al. [46] recorded AmO_{2-x} thermal conductivity data, towards which the data plateaued.

The melting temperature of $(\text{Am}_{0.80}\text{U}_{0.12}\text{Np}_{0.06}\text{Pu}_{0.02})\text{O}_{1.8}$ will need to be established in future experimental work for the ESA programme. Here, the melting temperatures of different americium/uranium oxides with cubic crystal structures are shown in Table 4. For this study, the lowest melting temperature is considered to see if fuel melting could be possible. Therefore, a temperature limit of 2260 K is considered here.

The curves generated by the analytical thermal model for the RTG under standard operation (Figure 6), and at high clad temperatures (Figure 9), are compared. The temperature difference between the maximum fuel temperature for a radiation-only case and conduction-only case is much smaller for the higher clad temperatures (see Figure 9) than the 623 K clad temperature (see Figure 6). This helps to constrain the possible range for the maximum fuel temperature.

Table 4. The melting temperatures of different cubic crystal structured americium/uranium oxides in the literature.

Oxide	Comment	Melting Temperature (K)	Reference
AmO ₂	The O/M after melting was not determined. Unlikely to be stoichiometric [53,54]	2386–2406	[10,36,53,55]
Am oxide with O/M ≤ 1.8	This is the oxygen to metal ratio of the oxide prior to a liquid phase [36].	2260	[10,36,54]
U _{0.33} Am _{0.67±0.02} O _{1.9}	The O/M ratio after melting was not determined.	2608 ± 52	[36]
UO ₂	N/A	3118 ± 28	[56]

The maximum fuel temperature will always be greater than the temperature of the inner surface of the clad. Figure 9a shows the first example of a higher clad temperature, $T_{i\ cl}$, 1750 K (This temperature was chosen as it results in a fuel temperature close to 1786 K—the highest temperature at which heat capacity data were determined. The fuel thermal conductivity could then be estimated using this experimental data.). The maximum fuel temperature could be approximately 1810 K in a radiation-only regime for an approximate fuel thermal conductivity of $0.86\text{ Wm}^{-1}\text{K}^{-1}$. The maximum fuel temperature is, therefore, lower than 2260 K—the lowest estimate for the fuel melting temperature from Table 4. In fact, Figure 9a illustrates that even if the fuel thermal conductivity is as low as 0.2, which is unlikely for $(\text{Am}_{0.80}\text{U}_{0.12}\text{Np}_{0.06}\text{Pu}_{0.02})\text{O}_{1.8}$, the maximum fuel temperature should not exceed around 1940 K. Similar figures for a clad temperature, $T_{i\ cl}$, of 1900 K and 1973 K are shown Figure 9b,c. Figure 9b illustrates that even if the thermal conductivity of the fuel is as low as $0.85\text{ Wm}^{-1}\text{K}^{-1}$, the maximum fuel temperature could be around 1955 K. This is about 300 K below the lowest estimate for the melting temperature (2260 K). Even if a less conservative thermal conductivity of $0.89\text{ Wm}^{-1}\text{K}^{-1}$ is assumed (see Section 3.3), the effect on the maximum fuel temperature would be negligible (decreasing it by 1 K). Figure 9b also shows that even if the fuel thermal conductivity is as low as $0.2\text{ Wm}^{-1}\text{K}^{-1}$, the maximum fuel temperature would only reach a maximum of $\sim 2085\text{ K}$. Finally, the maximum temperature that the clad is permitted to reach is considered for $T_{i\ cl}$, i.e. 1973 K. Figure 9c shows that if the thermal conductivity is assumed to be $0.8\text{ Wm}^{-1}\text{K}^{-1}$, the maximum temperature of the fuel is about 2030 K. This is about 230 K below the lowest estimate for the fuel's melting temperature. Although a thermal conductivity value slightly greater than $0.8\text{ Wm}^{-1}\text{K}^{-1}$ could be possible, e.g. $0.85\text{ Wm}^{-1}\text{K}^{-1}$, this has a negligible effect on the maximum fuel temperature (about 3 K decrease). To consider an extreme, if the fuel had a thermal conductivity of $0.2\text{ Wm}^{-1}\text{K}^{-1}$ (extremely unlikely for actinide oxides), Figure 9c shows that maximum fuel temperature would have been 2155 K—about 100 K less than the lowest estimate of the fuel melting temperature. Reaching such a thermal conductivity is extremely unlikely given the trend of Figure 8 and the general thermal conductivity values of actinide oxides. This study has shown that even with the new fuel, $(\text{Am}_{0.80}\text{U}_{0.12}\text{Np}_{0.06}\text{Pu}_{0.02})\text{O}_{1.8}$, the fuel will not melt in the ELHS based on the assumptions of this study even if the clad were to reach its maximum permitted temperature of 1973 K.

The ELHS requirement specifically states that the clad temperature must not be greater than 200 K below its melting point. It needs to be understood if a temperature margin will be required to limit the maximum fuel temperature based on the fuel's melting temperature. If it is required, this could impose a different maximum temperature limit on the clad depending on the size of the margin and the experimentally determined melting temperature of the fuel. For example, if the maximum fuel temperature is required to be no greater than 200 K below its melting temperature, and if the fuel melting temperature and fuel thermal conductivity are assumed to be 2260 K and $0.8\text{ Wm}^{-1}\text{K}^{-1}$, respectively, then a clad temperature of 1973 K will not be permitted. This is because the maximum fuel

temperature would only be 100 K below the melting temperature of the fuel. This study, therefore, highlighted:

1. The importance of establishing the melting temperature of the fuel.
2. The importance of deciding whether there needs to be a requirement for the maximum fuel temperature based on a margin below its melting temperature and, if so, the need to define the size of this margin.
3. The potential impact that point (2) could have on the maximum permitted clad temperature and, therefore, the need to review its current maximum temperature-imposed requirement.

Nonetheless, this investigation has highlighted that fuel melting will not occur based on the current requirements [12] that the fuel cannot reach its melting temperature, and that the clad is not permitted to exceed ~1973 K, as well as the assumptions of this study. Although this analytical thermal model could be adapted to reflect the RHU fuel geometry to estimate its maximum fuel temperature for a clad at 1973 K, it is already known that the RHU fuel will always be cooler than the ELHS fuel (owing to the different designs of the RHU and RTG/ELHS). Therefore, this study indirectly found that the RHU will not experience fuel melting. It has also found that the relative density of the sintered fuel form of RHU is not constrained by melting temperature concerns and an 80% T.D. should not be discounted if required. Nonetheless, the analytical thermal model can be adapted and used to determine the specific fuel temperatures under different clad temperatures if necessary.

Finally, it is important to highlight that it is unlikely that the fuel and clad will be in a radiation-only heat transfer regime as there will be at least some direct contact between the fuel and the clad, e.g. between the top and bottom of the cylindrical fuel volume and the clad. This means the maximum fuel temperature in practice will be even lower than that of a radiation-only regime and even lower than a fuel melting temperature. However, as Figure 9 shows, the difference between the maximum fuel temperature in a conduction-only regime and a radiation-only regime is small.

5. Conclusions

This study presented enthalpy and heat capacity data for the new prospect European RPS fuel ($\text{Am}_{0.80}\text{U}_{0.12}\text{Np}_{0.06}\text{Pu}_{0.02}\text{O}_{1.8}$) for the first time. The latter data are a vital step towards accurately determining thermal conductivity as a function of temperature for the fuel. It is recommended that the thermal diffusivity of the fuel and its thermal expansion be experimentally determined to allow the thermal conductivity to be accurately determined. Accurate thermal conductivity will be useful for future FE thermal analysis of the RPSs. The specific heat capacity data will also be useful for these studies. Heat capacity data will be informative for the future generation of a phase diagram for mixed americium uranium oxides. These studies will allow a greater understanding of the fuel under different conditions. It is also recommended that these investigations be conducted in the future if a higher purity fuel (without Np and Pu impurities) is made.

The ESA RPS programme is on a targeted timeline to launch the RPSs in the late 2020s and time will be required to acquire outstanding thermal diffusivity data and thermal expansion data for this new fuel. This study has presented a new analytical thermal model for the maximum fuel temperature of the ELHS (or RTG) as a function of fuel thermal conductivity. This has allowed different temperatures of the inner surface of the clad to be investigated; specifically, those that reflected the standard operation of the RTG and 1973 K, which corresponded to the current maximum permitted temperature according to the RPSs requirements [12]. The latter represents a hypothetical scenario. This analysis has enabled immediate insight into whether fuel melting could occur during such a scenario. This is the first known study (including for past fuels) in the RPS R&D programme to consider the effect of fuel relative density on the maximum fuel temperature. It has been found that an 80% T.D. sintered fuel will not cause fuel melting for a 1973 K clad inner surface temperature. To be conservative, the lowest melting temperature of americium/uranium oxides presented in the literature, namely, of americium oxide with O/M ≤ 1.8 , was

assumed. This analysis has been conducted with approximate lower estimates for the thermal conductivity of $(Am_{0.80}U_{0.12}Np_{0.06}Pu_{0.02})O_{1.8}$, which were made using lower confidence interval data for the experimental specific heat capacity data, and the lowest thermal diffusivity data for americium oxides in the literature, and assumptions for the fuels thermal expansion based on an Am-U oxide. Although the analysis has been conducted with approximate lower estimates for the fuel thermal conductivity, it was shown that fuel melting could not occur even if a lower thermal conductivity of $0.2 \text{ Wm}^{-1}\text{K}^{-1}$ was assumed. This is unrealistically low for actinide oxides even at 100% T.D. and would likely correspond to very low unrealistic relative densities, which would never be targeted for an RPS fuel. This key conclusion would have otherwise required waiting for the remaining data to determine the thermal conductivity of the fuel to be completed over the coming years. This is an extremely beneficial insight for the ESA RPS programme as it presents no concerns for the current RPS and fuel R&D with the new $(Am_{0.80}U_{0.12}Np_{0.06}Pu_{0.02})O_{1.8}$ fuel, as a realistic lower relative density limit of 80% T.D. has not been discounted. It can, therefore, be considered in future sintering studies or helium outgassing investigations that will occur over the coming years. This study has also highlighted a question: whether a margin may be required that imposes a maximum temperature for the fuel that is less than its melting temperature. This will warrant further consideration. Depending on the margin, the melting temperature of the fuel, the actual clad temperatures for different extreme temperature accidents, and the exact thermal conductivity, it is possible that a clad inner surface temperature of less than 1973 K may be required and that the current RPS requirements [12] may need to be reviewed. Results of the ongoing fuel-clad chemical interaction study by Watkinson et al. may also affect this value.

This analytical thermal model can be used in the future to investigate the effect of updated RTG or ELHS designs on the maximum fuel temperature of the RTG during standard operation. Here, it was estimated that the maximum temperature of the fuel in RTG could be no greater than around 1250 K. Using this upper limit to constrain the lowest thermal conductivity based on lowest thermal conductivity value estimates for the $(Am_{0.80}U_{0.12}Np_{0.06}Pu_{0.02})O_{1.8}$ fuel (based on the thermal diffusivity of AmO_{2-x} and the lower confidence interval of the heat capacity data), it was estimated that the maximum temperature of the fuel in a radiation-only regime would be about 1120 K. This is an informative result.

The analytical thermal model is a general tool. It could be used to investigate the maximum fuel temperature for future generations of the RTG/ELHS with different fuel dimensions or even different fuels by varying some of the parameters, e.g. power density, fuel dimensions or thermal conductivity. The model allows the general effect of fuel thermal conductivity to be investigated easily and quickly. The model can also be used for current and future RHUs in a similar way.

In summary, given that fuel melting will not occur, it is recommended that relative densities below the current RPS fuel density range of 85–95% T.D. not be discounted for the RTG/ELHS and the RHU if greater porosity may need to be investigated for other research purposes, e.g. helium outgassing. It is also recommended that the following properties be determined for this fuel:

- Melting temperature using a laser flash method (details of the method can be found in [36]).
- Lattice parameter thermal expansion data by high temperature X-ray diffraction. These data can be used to estimate bulk/macrosopic volume thermal expansion as a function of temperature.
- Thermal diffusivity up to the melting temperature, which may require a standard laser flash method and a specialised laser flash method to reach temperatures above 1550 K [48].

These parameters may also need to be investigated for the oxidised fuel form as the fuel may experience oxidation under certain accidents.

It is noted that the RPSs operate (under standard operation conditions) at lower temperatures where self-irradiation induced defects will likely remain in the fuel. Future work should investigate the influence of this effect on the fuel lattice expansion at RPSs' operational temperatures. Similarly, future investigations should also include helium accumulation and outgassing studies in the fuel, as well the potential for pellet swelling at operational temperatures. The lattice expansion associated with defects and helium could cause a reduction in thermal conductivity at lower temperatures, as noted by studies with minor actinide bearing fuels [57,58]. Similarly, as was noted by others [23], self-irradiation can influence the heat capacity of a material. It is recommended that the effect of self-irradiation on the heat capacity of this fuel at lower temperatures should be investigated as part of future work. Finally, the effect of the size of the sintered grains on heat capacity could also be studied.

Supplementary Materials: The following are available online at <https://www.mdpi.com/article/10.3390/thermo1030020/s1>. Table S1: Low Temperature Heat Capacity Data.

Author Contributions: Conceptualisation, E.J.W., J.-F.V., R.M., O.B. and R.M.A.; methodology, R.M., O.B., M.S., J.-C.G., E.C., E.J.W. and J.-F.V.; software, R.M.; validation, D.S.; formal analysis, E.J.W., J.-F.V., J.-C.G. and E.C.; investigation, E.J.W., J.-F.V., J.-C.G., E.C., M.S., O.B. and R.M.; resources, O.B., M.S., J.-C.G., E.C., R.J.M.K. and J.-F.V.; data curation, J.-F.V., E.J.W., R.M., J.-C.G. and E.C.; writing—original draft preparation, E.J.W., J.-F.V., J.-C.G., E.C., R.M. and O.B.; writing—review and editing, E.J.W., J.-F.V., O.B., J.-C.G., E.C., D.F., R.M., D.S. and R.J.M.K.; visualisation, E.J.W., J.-F.V., R.M., J.-C.G. and E.C.; supervision, R.M.A., R.J.M.K., D.F. and O.B.; project administration, R.M.A., R.J.M.K. and D.F.; funding acquisition, R.M.A. and R.J.M.K. All authors have read and agreed to the published version of the manuscript.

Funding: This research was funded by a number of entities. E. J. Watkinson wishes to acknowledge the Visiting Scientist agreement that has enabled the collaboration with EC JRC Karlsruhe. The University of Leicester acknowledges its significant in-kind contribution that paid for the time for E. J. Watkinson to work on this research, and the majority of travel and associated access costs for this collaboration. The University of Leicester also wishes to acknowledge the National Nuclear Laboratory for the provision of a contribution to the research travel and subsistence costs, as part of an ESA-funded programme. The University of Leicester acknowledges funding and support by the European Space Agency to pursue this research more widely, particularly of Keith Stephenson. ESA contract no.: 4000125885. Part of this research was funded by the H2020 EURATOM Research and Training Programme.

Institutional Review Board Statement: Not applicable.

Informed Consent Statement: Not applicable.

Data Availability Statement: Data are contained within the article or Supplementary Materials.

Acknowledgments: E.J. Watkinson wishes to acknowledge the Visiting Scientist agreement that has enabled the collaboration with EC JRC Karlsruhe, the experimental activity at EC JRC Karlsruhe, the opportunity and use of EC JRC Karlsruhe facilities and the technical support enabled by this collaboration. The University of Leicester would also like to acknowledge the significant in-kind contribution from the EC JRC Karlsruhe team. The authors would also like to acknowledge relevant RPS discussions with A. Barco (University of Leicester).

Conflicts of Interest: The authors declare no conflict of interest.

Appendix A. Debye and Einstein Function Fit to Low Temperature Heat Capacity Data

The heat capacity function that combines Debye and Einstein functions is:

$$C_p = n_D D(\theta_D) + n_E E(\theta_E) \quad (\text{A1})$$

where the total number of atoms in the formula, $(\text{Am}_{0.80}\text{U}_{0.12}\text{Np}_{0.06}\text{Pu}_{0.02})\text{O}_{1.8}$, is approximately equal to the total of n_D and n_E , and where

$$D(\theta_D) = 9R \left(\frac{1}{x}\right)^3 \int_0^x \frac{e^x x^4}{(e^x - 1)^2} dx, \text{ where } x = \frac{\theta_D}{T} \quad (\text{A2})$$

and

$$E(\theta_E) = 3Ry^2 \frac{e^y}{(e^y - 1)^2}, \text{ where } y = \frac{\theta_E}{T} \quad (\text{A3})$$

R is the universal gas constant and T is the temperature. Further details of this relationship can be found in Smith et al. [59].

The low temperature heat capacity data is fitted well to this combined heat capacity Equation (A1), as shown in Figure A1. Table A1 notes the determined parameters. It can be seen that the summation of n_D and n_E is 2.1, which is close to the total number of atoms.

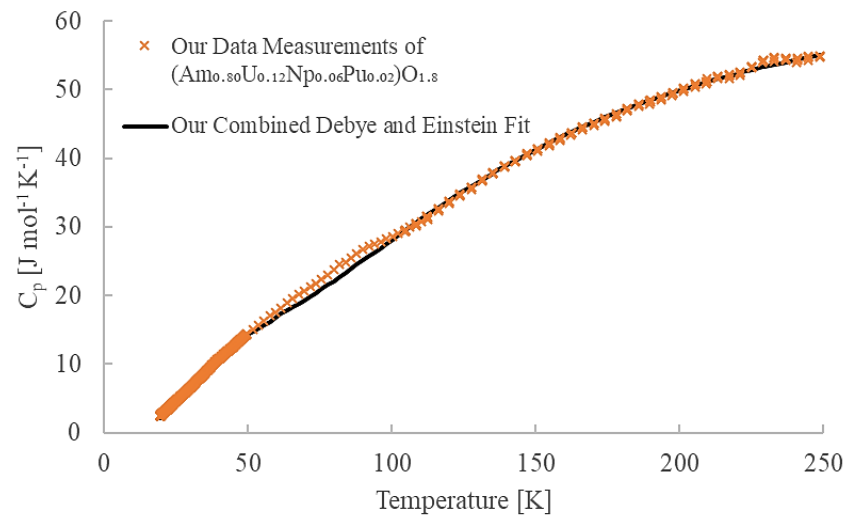


Figure A1. The combined Debye and Einstein heat capacity functions fit with the low temperature heat capacity data for $(\text{Am}_{0.80}\text{U}_{0.12}\text{Np}_{0.06}\text{Pu}_{0.02})\text{O}_{1.8}$.

Table A1. The parameters of the combined Debye and Einstein heat capacity functions fit.

Parameter	Fitted Value
n_D	0.3
n_E	1.8
T_D	115 K
T_E	479 K

Appendix B. The Fuel Steady-State Temperature Model

The steady-state thermal model of a cylindrical fuel pellet, with a diameter of $2a$, height $2l$ and uniform heat generation \dot{q} , can be represented as a quarter model bound by a uniform outer surface temperature T_s and zero temperature gradient boundary conditions. The reader is referred to Figure A2.

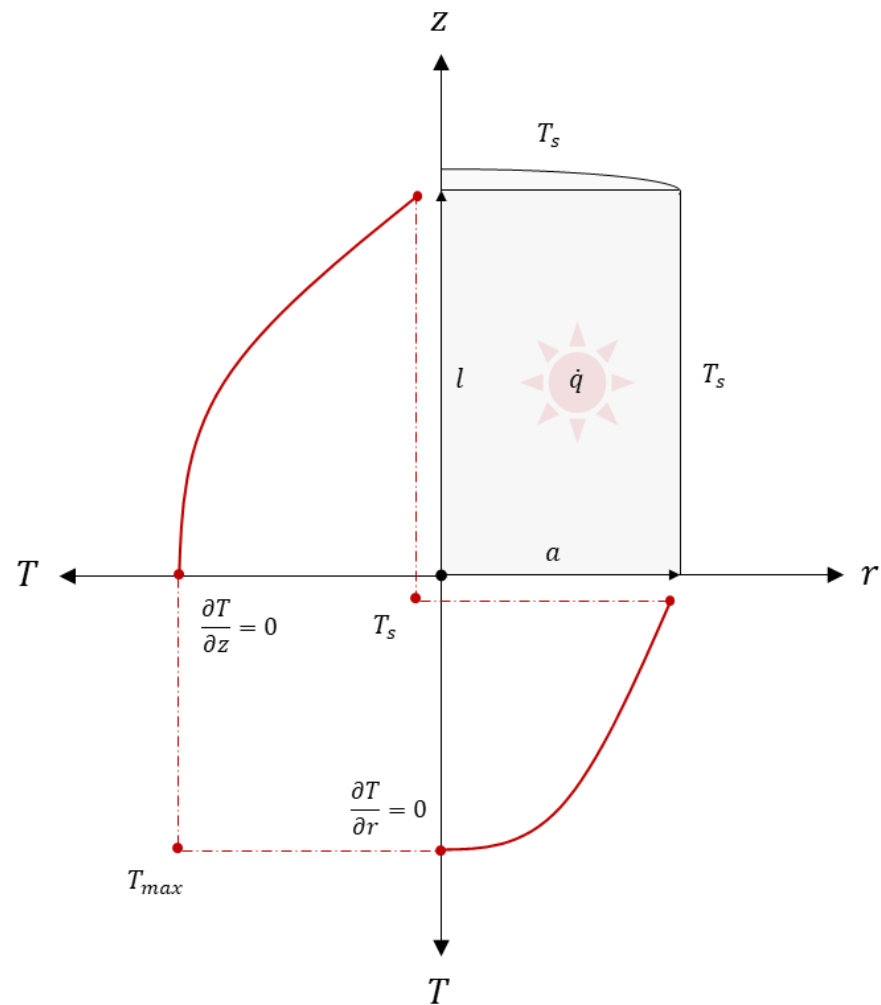


Figure A2. Thermal model of a cylindrical fuel pellet with internal heat generation and uniform outer surface temperature.

The governing equation for the steady-state thermal model described above can be written in the form of Poisson's equation in two-dimensional space using cylindrical and axial coordinates:

$$\frac{1}{r} \frac{\partial}{\partial r} \left(r \frac{\partial T}{\partial r} \right) + \frac{\partial^2 T}{\partial z^2} + \frac{\dot{q}}{k} = 0, \quad 0 < z < l, \quad 0 < r < a \quad (\text{A4})$$

where the following Dirichlet and Neumann boundary conditions are:

$$\frac{\partial T}{\partial z} = 0, \quad z = 0, \quad 0 < r < a \quad (\text{A5})$$

$$T = T_s, \quad z = l, \quad 0 < r < a \quad (\text{A6})$$

$$\frac{\partial T}{\partial r} = 0, \quad r = 0, \quad 0 < z < l \quad (\text{A7})$$

$$T = T_s, \quad r = a, \quad 0 < z < l \quad (\text{A8})$$

While all of these expressions are linear, some are inhomogeneous. To overcome this, the temperature variable is normalised in terms of temperature difference:

$$\theta = T - T_s \quad (\text{A9})$$

The governing equation therefore becomes:

$$\frac{1}{r} \frac{\partial}{\partial r} \left(r \frac{\partial \theta}{\partial r} \right) + \frac{\partial^2 \theta}{\partial z^2} + \frac{\dot{q}}{k} = 0, \quad 0 < z < l, \quad 0 < r < a, \quad (\text{A10})$$

with the new homogenous boundary conditions being:

$$\frac{\partial \theta}{\partial z} = 0, \quad z = 0, \quad 0 < r < a \quad (\text{A11})$$

$$\theta = 0, \quad z = l, \quad 0 < r < a \quad (\text{A12})$$

$$\frac{\partial \theta}{\partial r} = 0, \quad r = 0, \quad 0 < z < l \quad (\text{A13})$$

$$\theta = 0, \quad r = a, \quad 0 < z < l \quad (\text{A14})$$

To solve the inhomogeneous partial differential equation, a solution of the form is assumed:

$$\theta(z, r) = \varphi(z) + \psi(z, r) \quad (\text{A15})$$

where $\varphi(z)$ is chosen to absorb the uniform heat generation term in the partial differential equation and is thus the solution of the following ordinary differential equation problem:

$$\theta(z, r) = \varphi(z) + \psi(z, r) \quad (\text{A16})$$

$$\frac{\partial \varphi}{\partial z} = 0, \quad z = 0 \quad (\text{A17})$$

$$\varphi = 0, \quad z = l \quad (\text{A18})$$

By integrating twice and determining the integration constants using the appropriate boundary conditions, the solution for $\varphi(z)$ is simply:

$$\varphi(z) = \frac{\dot{q}l^2}{2k} \left(1 - \frac{z^2}{l^2} \right) \quad (\text{A19})$$

On the other hand, $\psi(z, r)$ is the solution of the following problem:

$$\frac{1}{r} \frac{\partial}{\partial r} \left(r \frac{\partial \psi}{\partial r} \right) + \frac{\partial^2 \psi}{\partial z^2} = 0, \quad 0 < z < l, \quad 0 < r < a \quad (\text{A20})$$

$$\frac{\partial \psi}{\partial z} = 0, \quad z = 0, \quad 0 < r < a \quad (\text{A21})$$

$$\psi = 0, \quad z = l, \quad 0 < r < a \quad (\text{A22})$$

$$\frac{\partial \psi}{\partial r} = 0, \quad r = 0, \quad 0 < z < l \quad (\text{A23})$$

$$\psi = -\varphi, \quad r = a, \quad 0 < z < l \quad (\text{A24})$$

As is evident from the above, the problem for $\psi(z, r)$ has a homogenous differential equation and an inhomogeneous boundary condition at $r = a$. Hence, the problem can be solved directly via the separation of variables, where a solution of the following form is assumed:

$$\psi(z, r) = R(r)Z(z) \quad (\text{A25})$$

Substituting this into the partial differential equation yields two ordinary differential equations:

$$\frac{\partial^2 Z}{\partial z^2} + \lambda^2 Z = 0, \quad 0 < z < l \quad (\text{A26})$$

$$\frac{\partial^2 R}{\partial r^2} + \frac{1}{r} \frac{\partial R}{\partial r} - \lambda^2 R = 0, \quad 0 < r < a, \quad (\text{A27})$$

where λ is the separation constant to be determined.

The general solutions for the two ordinary differential equations can be written in the form:

$$Z(z) = C_1 \cos \lambda z + C_2 \sin \lambda z \quad (\text{A28})$$

$$R(r) = C_3 I_0(\lambda r) + C_4 K_0(\lambda r) \quad (\text{A29})$$

where C_1 , C_2 , C_3 and C_4 are integral constants to be determined, while I_0 and K_0 are modified (hyperbolic) Bessel functions of the first and second kind, respectively.

The homogenous direction of the problem is z . In view of the boundary conditions at $z = 0$, the eigenfunction will be:

$$Z(z) = C_1 \cos \lambda z \quad (\text{A30})$$

while the boundary condition at $z = l$ delivers the eigencondition:

$$\cos \lambda l = 0 \longrightarrow \lambda_n = \frac{1}{2l}(2n - 1)\pi, \quad n = 1, 2, \dots, \quad (\text{A31})$$

where the specific case of $\lambda_n = 0$ does not contribute to the solution.

On the other hand, the boundary condition at $r = 0$ will lead to $K_0 \rightarrow \infty$, and thus, cannot be part of a physically acceptable solution. Hence, the general solution to $\psi(z, r)$ takes the form:

$$\cos \lambda l = 0 \longrightarrow \lambda_n = \frac{1}{2l}(2n - 1)\pi, \quad n = 1, 2, \dots, \quad (\text{A32})$$

where $C_n = C_1 C_3$.

Application of the boundary condition at $r = a$ gives:

$$-\varphi(z) = \sum_{n=1}^{\infty} C_n I_0(\lambda_n a) \cos \lambda_n z \quad (\text{A33})$$

from which an expression for C_n can be obtained using the orthogonality properties of the eigenfunctions:

$$\begin{aligned} C_n &= -\frac{\int_0^l \varphi \cos \lambda_n z dz}{I_0(\lambda_n a) \int_0^l \cos^2 \lambda_n z dz} \\ &= -\frac{2}{I_0(\lambda_n a)} \int_0^l \varphi \cos \lambda_n z dz \end{aligned} \quad (\text{A34})$$

The remaining integral is evaluated using integration by parts:

$$\begin{aligned} \int_0^l \varphi \cos \lambda_n z dz &= -\frac{1}{\lambda_n^2} \int_0^l \varphi \frac{\partial^2}{\partial z^2} (\cos \lambda_n z) dz \\ &= -\frac{1}{\lambda_n^2} \left[\varphi \frac{\partial}{\partial z} (\cos \lambda_n z) \Big|_0^l - \frac{\partial \varphi}{\partial z} \cos \lambda_n z \Big|_0^l + \int_0^l \frac{\partial^2 \varphi}{\partial z^2} \cos \lambda_n z dz \right] \\ &= \frac{\dot{q}}{k \lambda_n^2} \int_0^l \cos \lambda_n z dz = \frac{\dot{q}}{k \lambda_n^3} \sin \lambda_n l \\ &= -\frac{\dot{q}}{k \lambda_n^3} (-1)^n \end{aligned} \quad (\text{A35})$$

whereupon the following final solution is obtained:

$$T(z, r) = T_s + \frac{\dot{q} l^2}{2k} \left[1 - \frac{z^2}{l^2} + \sum_{n=1}^{\infty} \frac{4(-1)^n}{\lambda_n^3 l^3 I_0(\lambda_n a)} I_0(\lambda_n r) \cos \lambda_n z \right] \quad (\text{A36})$$

The maximum temperature at the centre of the fuel pellet can, therefore, be written as:

$$T_{max} = T(0, 0) = T_s + \frac{\dot{q} l^2}{2k} \left[1 + \sum_{n=1}^{\infty} \frac{4(-1)^n}{\lambda_n^3 l^3 I_0(\lambda_n a)} \right] \quad (\text{A37})$$

Appendix C. Data Extraction and Power Law Fit of AmO_{2-x} Thermal Diffusivity Data by Nishi et al.

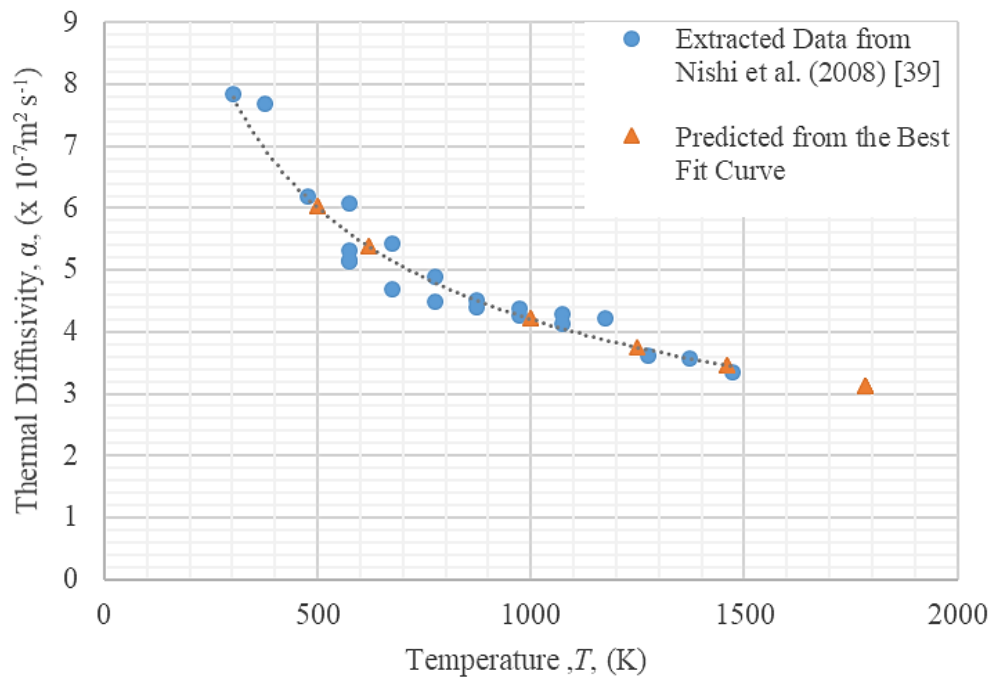


Figure A3. The thermal diffusivity data as a function of temperature extracted data from Nishi et al. [47] (●), presented using WebPlotDigitizer [49], together with the power law line of best fit (●). Values predicted at different temperatures from the curve are shown including extrapolated values at 1785 K (▲).

The equation of best fit of the thermal diffusivity, α , as a function of temperature, T , is:

$$\alpha = 1.4781 \times 10^{-5} T^{-0.515} \quad (\text{A38})$$

References

1. Summerer, L.; Stephenson, K. Nuclear power sources: A key enabling technology for planetary exploration. *Proc. Inst. Mech. Eng. G J. Aerosp. Eng.* **2011**, *225*, 129–143. [CrossRef]
2. Ambrosi, R.M.; Williams, H.R.; Samara-Ratna, P.; Bannister, N.P.; Vernon, D.; Crawford, T.; Bicknell, C.; Jordan, A.; Slade, R.; Deacon, T.; et al. Development and testing of americium-241 radioisotope thermoelectric generator: Concept designs and breadboard system. In Proceedings of the Nuclear and Emerging Technologies for Space, The Woodlands, TX, USA, 21–23 March 2012.
3. Williams, H.R.; Ambrosi, R.M.; Bannister, N.P.; Samara-Ratna, P.; Sykes, J. A conceptual spacecraft radioisotope thermoelectric and heating unit (RTHU). *Int. J. Energy Res.* **2012**, *36*, 1192–1200. [CrossRef]
4. Ambrosi, R.M.; Williams, H.; Watkinson, E.J.; Barco, A.; Mesalam, R.; Crawford, T.; Bicknell, C.; Samara-Ratna, P.; Vernon, D.; Bannister, N.; et al. European radioisotope thermoelectric generators (RTGs) and radioisotope heater units (RHUs) for space science and exploration. *Space Sci. Rev.* **2019**, *215*, 55. [CrossRef]
5. Brown, J.; Campbell, C.; Carrigan, C.; Carrott, M.; Greenough, K.; Maher, C.; McLuckie, B.; Mason, C.; Gregson, C.; Griffiths, T.; et al. Americium and plutonium purification by extraction (the AMPPEX process): Development of a new method to separate ²⁴¹Am from aged plutonium dioxide for use in space power systems. *Prog. Nucl. Energy* **2018**, *106*, 396–416. [CrossRef]
6. Sarsfield, M.J.; Fenwick, H.; Glenville, P.; Kramer, D.P.; Watkinson, E.J.; Ambrosi, R.M.; Williams, H.R.; Barklay, C.D.; Stephenson, K.; Tinsley, T. Sintering and characterisation of cerium dioxide as a surrogate for americium-241 #6079. In Proceedings of the Nuclear and Emerging Technologies for Space (NETS), Huntsville, AL, USA, 22–25 February 2016.
7. Watkinson, E.J.; Ambrosi, R.M.; Williams, H.R.; Sarsfield, M.J.; Stephenson, K.; Weston, D.P.; Marsh, N.; Haidon, C. Cerium neodymium oxide solid solution synthesis as a potential analogue for substoichiometric AmO₂ for radioisotope power systems. *J. Nucl. Mater.* **2017**, *486*, 308–322. [CrossRef]
8. Watkinson, E.J.; Ambrosi, R.M.; Kramer, D.P.; Williams, H.R.; Reece, M.J.; Chen, K.; Sarsfield, M.J.; Barklay, C.D.; Fenwick, H.; Weston, D.P.; et al. Sintering trials of analogues of americium oxides for radioisotope power systems. *J. Nucl. Mater.* **2017**, *491*, 18–30. [CrossRef]

9. Sarsfield, M.J.; Campbell, C.; Carrigan, C.; Carrott, M.J.; Colle, J.-Y.; Freis, D.; Gregson, C.; Griffiths, T.; Holt, J.; Lajarge, P.; et al. The separation of 241Am from aged plutonium dioxide for use in radioisotope power systems #1030. In Proceedings of the European Space Power Conference, Thessaloniki, Greece, 3–7 October 2016.
10. Epifano, E.; Guéneau, C.; Belin, R.C.; Vauchy, R.; Lebreton, F.; Richaud, J.-C.; Joly, A.; Valot, C.; Martin, P.M. Insight into the Am–O phase equilibria: A thermodynamic study coupling high-temperature XRD and CALPHAD modeling. *Inorg. Chem.* **2017**, *56*, 7416–7432. [[CrossRef](#)] [[PubMed](#)]
11. Vigier, J.-F.; Freis, D.; Pöml, P.; Prieur, D.; Lajarge, P.; Gardeur, S.; Guiot, A.; Bouëxière, D.; Konings, R.J.M. Optimization of uranium-doped americium oxide synthesis for space application. *Inorg. Chem.* **2018**, *57*, 4317–4327. [[CrossRef](#)] [[PubMed](#)]
12. University of Leicester. *TN2 RTG Requirements Specification, UL-RTG-TN-001*; University of Leicester: Leicester, UK, 2021.
13. The PGM Database, T.P. Platinum-20.00% Rhodium. Available online: <http://www.pgmdatabase.com/jmpgm/index.jsp> (accessed on 17 June 2021).
14. Erdmann, B.; Keller, C. The preparation of actinide (+ zirconium and hafnium)-noble metal alloy phases by coupled reductions. *Inorg. Nucl. Chem. Lett.* **1971**, *7*, 675–683. [[CrossRef](#)]
15. Schulz, W.W. *Chemistry of Americium*; Technical Information Center Energy Research and Development Administration: Oak Ridge, TN, USA, 1976. [[CrossRef](#)]
16. Watkinson, E.J.; Cremer, B.; Lajarge, P.; Gardeur, P.; Vigier, J.-F.; Berkmann, C.; Ernstberger, M.; Wiss, T.; Freis, D.; Crawford, T.; et al. Americium-based oxide and Pt-Rh alloys compatibility/interaction tests in the context of European space radioisotope power systems. In Proceedings of the Nuclear and Emerging Technologies for Space (NETS) 2020, Knoxville, TN, USA, 6–9 April 2020; p. 24.
17. Epifano, E.; Beneš, O.; Vălu, O.S.; Zappey, J.; Lebreton, F.; Martin, P.M.; Guéneau, C.; Konings, R.J.M. High temperature heat capacity of (U, Am)O₂ ± x. *J. Nucl. Mater.* **2017**, *494*, 95–102. [[CrossRef](#)]
18. Vălu, O.S.; Staicu, D.; Beneš, O.; Konings, R.J.M.; Lajarge, P. Heat capacity, thermal conductivity and thermal diffusivity of uranium–americium mixed oxides. *J. Alloy. Compd.* **2014**, *614*, 144–150. [[CrossRef](#)]
19. Nishi, T.; Itoh, A.; Ichise, K.; Arai, Y. Heat capacities and thermal conductivities of AmO₂ and AmO. *J. Nucl. Mater.* **2011**, *414*, 109–113. [[CrossRef](#)]
20. Jossou, E.; Malakkal, L.; Ranasingh, J.; Szpunar, B.; Szpunar, J. Thermophysical properties of (U_xAm_{1-x})O₂ MOX fuel. *Comput. Mater. Sci.* **2020**, *172*, 109324. [[CrossRef](#)]
21. Bromley, B.P.; Colton, A.V. Reactor physics assessment of potential feasibility of using advanced, nonconventional fuels in a pressure tube heavy water reactor to destroy Americium and Curium. *Nucl. Technol.* **2021**, *207*, 1193–1215. [[CrossRef](#)]
22. Tyrpekl, V.; Holzhäuser, M.; Hein, H.; Vigier, J.-F.; Somers, J.; Svora, P. Synthesis of dense yttrium-stabilised hafnia pellets for nuclear applications by spark plasma sintering. *J. Nucl. Mater.* **2014**, *454*, 398–404. [[CrossRef](#)]
23. Vălu, O.S.; Beneš, O.; Colineau, E.; Griveau, J.C.; Konings, R.J.M. The low-temperature heat capacity of (U_{1-y}Am_y)O_{2-x} for y = 0.08 and 0. *J. Nucl. Mater.* **2018**, *507*, 126–134. [[CrossRef](#)]
24. Lashley, J.C.; Hundley, M.F.; Migliori, A.; Sarrao, J.L.; Pagliuso, P.G.; Darling, T.W.; Jaime, M.; Cooley, J.C.; Hults, W.L.; Morales, L.; et al. Critical examination of heat capacity measurements made on a Quantum Design physical property measurement system. *Cryogenics* **2003**, *43*, 369–378. [[CrossRef](#)]
25. Javorský, P.; Wastin, F.; Colineau, E.; Rebizant, J.; Boulet, P.; Stewart, G. Low-temperature heat capacity measurements on encapsulated transuranium samples. *J. Nucl. Mater.* **2005**, *344*, 50–55. [[CrossRef](#)]
26. Javorský, P. *Low-Temperature Specific Heat Measurements on Transuranium Samples (Final Report)*; JRC-ITU-TN-2004/11 and JRC14988; European Commission, Joint Research Centre, Institute for Transuranium Elements: Karlsruhe, Germany, 2004.
27. Beneš, O.; Gotcu-Freis, P.; Schwörer, F.; Konings, R.J.M.; Fanghänel, T. The high temperature heat capacity of NpO. *J. Chem. Thermodyn.* **2011**, *43*, 651–655. [[CrossRef](#)]
28. Beneš, O. Thermodynamics of Molten Salts for Nuclear Applications. Ph.D. Thesis, Institute of Chemical Technology, Prague, Czech Republic, 2008.
29. Wilkins, S.B.; Caciuffo, R.; Detlefs, C.; Rebizant, J.; Colineau, E.; Wastin, F.; Lander, G.H. Direct observation of electric-quadrupolar order in UO₂. *Phys. Rev. B* **2006**, *73*, 060406. [[CrossRef](#)]
30. Santini, P.; Carretta, S.; Magnani, N.; Amoretti, G.; Caciuffo, R. Hidden order and low-energy excitations in NpO₂. *Phys. Rev. Lett.* **2006**, *97*, 207203. [[CrossRef](#)]
31. Martel, L.; Hen, A.; Tokunaga, Y.; Kinnart, F.; Magnani, N.; Colineau, E.; Griveau, J.-C.; Caciuffo, R. Magnetization, specific heat, ¹⁷O NMR, and ²³⁷Np Mössbauer study of U_{0.15}Np_{0.85}O₂. *Phys. Rev. B* **2018**, *98*, 014410. [[CrossRef](#)]
32. Fink, J.K. Thermophysical properties of uranium dioxide. *J. Nucl. Mater.* **2000**, *279*, 1–18. [[CrossRef](#)]
33. Konings, R.J.M.; Beneš, O.; Kovács, A.; Manara, D.; Sedmidubský, D.; Gorokhov, L.; Iorish, V.S.; Yungman, V.; Shenyavskaya, E.; Osina, E. The thermodynamic properties of the f-elements and their compounds. Part 2 the lanthanide and actinide oxides. *J. Phys. Chem. Ref. Data* **2014**, *43*, 013101. [[CrossRef](#)]
34. Epifano, E.; Naji, M.; Manara, D.; Scheinost, A.C.; Hennig, C.; Lechelle, J.; Konings, R.J.M.; Guéneau, C.; Prieur, D.; Vitova, T.; et al. Extreme multi-valence states in mixed actinide oxides. *Commun. Chem.* **2019**, *2*, 59. [[CrossRef](#)]
35. Manikandan, G.; Murugan, G.; Raghukandan, K. Effect of grain size upon the thermal behavior of copper and diamond powders using differential scanning calorimetry (DSC). *Indian J. Sci. Technol.* **2016**, *9*, 1–4. [[CrossRef](#)]

36. Epifano, E.; Prieur, D.; Martin, P.M.; Guéneau, C.; Dardenne, K.; Rothe, J.; Vitova, T.; Dieste, O.; Wiss, T.; Konings, R.J.M.; et al. Melting behaviour of uranium-amerium mixed oxides under different atmospheres. *J. Chem. Thermodyn.* **2020**, *140*, 105896. [[CrossRef](#)]
37. De Bruycker, F.; Boboridis, K.; Manara, D.; Pöml, P.; Rini, M.; Konings, R.J.M. Reassessing the melting temperature of PuO₂. *Mater. Today* **2010**, *13*, 52–55. [[CrossRef](#)]
38. Böhler, R.; Welland, M.J.; Prieur, D.; Cakir, P.; Vitova, T.; Pruessmann, T.; Pidchenko, I.; Hennig, C.; Guéneau, C.; Konings, R.J.M.; et al. Recent advances in the study of the UO₂–PuO₂ phase diagram at high temperatures. *J. Nucl. Mater.* **2014**, *448*, 330–339. [[CrossRef](#)]
39. Kaye, G.W.C.; Laby, T.H. *Tables of Physical and Chemical Constants*, 14th ed.; Longman: Harlow, UK, 1973.
40. The PGM Database, T.P. Notes For Emissivity Attribute of Rhodium. Available online: <http://www.pgmdatabase.com/jmpgm/index.jsp> (accessed on 16 June 2021).
41. Foote, D.P. The emissivity of metals and oxides. III. The total emissivity of platinum and the relation between total emissivity and resistivity. *Bull. Bur. Stand.* **1915**, *11*, 607–612.
42. Bradley, D.; Entwistle, A.G. Determination of the emissivity, for total radiation, of small diameter platinum-10% rhodium wires in the temperature range 600–1450 °C. *Br. J. Appl. Phys.* **1961**, *12*, 708–711. [[CrossRef](#)]
43. Transmetra. *Table of Emissivity of Various Surfaces*; Transmetra: Flurlingen, Switzerland, 2012; Available online: https://www.transmetra.ch/images/transmetra_pdf/publikationen_literatur/pyrometrie-thermografie/emissivity_table.pdf (accessed on 16 June 2021).
44. McElroy, D.L.; Kollie, T.G. The total hemispherical emittance of platinum, Columbium-1% Zirconium, and polished and oxidized Inor-8 in the range 100 °C to 1200 °C. In *Measurement of Thermal Radiation Properties of Solids*. NASA SP-31; Richmond, J.C., Ed.; National Aeronautics and Space Administration: Hampton, VA, USA, 1963; pp. 365–377.
45. Phillips, D.G. *Technology Development of a Biowaste Resistojet*; National Aeronautics and Space Administration Langley Research Center: Hampton, VA, USA, 1972; Volume 1.
46. Nishi, T.; Takano, M.; Itoh, A.; Akabori, M.; Arai, Y.; Minato, K.; Numata, M. Thermal conductivity of AmO_{2-x}. *J. Nucl. Mater.* **2008**, *373*, 295–298. [[CrossRef](#)]
47. Nishi, T.; Itoh, A.; Takano, M.; Akabori, M.; Arai, Y.; Minato, K. Thermal conductivities of minor actinide oxides for advanced fuel. In Proceedings of the ATALANTE 2008, Montpellier, France, 19–22 May 2008.
48. Vlahovic, L.; Staicu, D.; Küst, A.; Konings, R.J.M. Thermal diffusivity of UO₂ up to the melting point. *J. Nucl. Mater.* **2018**, *499*, 504–511. [[CrossRef](#)]
49. Rohatgi, A. WebPlotDigitizer, Version: 4.4. (November 2020). Rohatgi: Pacifica, CA, USA. Available online: <https://automeris.io/WebPlotDigitizer>.
50. Lebreton, F.; Belin, R.C.; Delahaye, T.; Blanchart, P. In-situ X-ray diffraction study of phase transformations in the Am–O system. *J. Solid State Chem.* **2012**, *196*, 217–224. [[CrossRef](#)]
51. Epifano, E.; Vauchy, R.; Lebreton, F.; Joly, A.; Guéneau, C.; Valot, C.; Martin, P.M. Behaviour of (U,Am)O₂ in oxidizing conditions: A high-temperature XRD study. *J. Nucl. Mater.* **2020**, *531*, 151991. [[CrossRef](#)]
52. Schulz, B. Thermal conductivity of porous and highly porous materials. *High Temp. High Press.* **1981**, *13*, 649–660.
53. McHenry, R.E. Melting points of curium and americium oxides. *Trans. Am. Nucl. Soc.* **1965**, *8*, 75–76.
54. Gotcu-Freis, P.; Colle, J.Y.; Guéneau, C.; Dupin, N.; Sundman, B.; Konings, R.J.M. A thermodynamic study of the Pu–Am–O system. *J. Nucl. Mater.* **2011**, *414*, 408–421. [[CrossRef](#)]
55. Freis, D.; Vigier, J.; Popa, K.; Konings, R. Research in support of European Radioisotope Power System development at the European Commission’s Joint Research Centre in Karlsruhe. *ATW Int. J. Nucl. Power* **2020**, *65*, 198–205.
56. Pavlov, T.; Vlahovic, L.; Staicu, D.; Konings, R.J.M.; Wenman, M.R.; Grimes, R.W.; Van Uffelen, P. Experimental evaluation of the high temperature thermophysical properties of UO₂. In Proceedings of the Top Fuel 2016: LWR Fuels with Enhanced Safety and Performance, Boise, ID, USA, 11–15 September 2016; pp. 1227–1235.
57. Takano, M.; Akabori, M.; Arai, Y. Annealing behavior of (Pu,Cm)O₂ lattice and bulk expansion from self-irradiation damage. *J. Nucl. Mater.* **2011**, *414*, 174–178. [[CrossRef](#)]
58. Nishi, T.; Takano, M.; Akabori, M.; Arai, Y. Thermal conductivity of (Np_{0.20}Pu_{0.50}Am_{0.25}Cm_{0.05})O_{2-x} solid solutions. *J. Nucl. Mater.* **2013**, *440*, 534–538. [[CrossRef](#)]
59. Smith, A.L.; Griveau, J.C.; Colineau, E.; Raison, P.E.; Wallez, G.; Konings, R.J.M. Low temperature heat capacity of Na₄UO₅ and Na₄NpO₅. *J. Chem. Thermodyn.* **2015**, *91*, 245–255. [[CrossRef](#)]